Superfluid vortex multipoles and soliton stripes on a torus

J. D'Ambroise,[1] R. Carretero-González,[2] P. Schmelcher,[3,4] and P. G. Kevrekidis[5]

[1]*Department of Mathematics, Computer & Information Science, State University of New York at Old Westbury, Westbury, New York 11568, USA*

[2]*Nonlinear Dynamical Systems Group, Computational Sciences Research Center, and Department of Mathematics and Statistics, San Diego State University, San Diego, California 92182-7720, USA*

[3]*Center for Optical Quantum Technologies, Department of Physics, University of Hamburg, Luruper Chaussee 149, 22761 Hamburg, Germany*

[4]*The Hamburg Centre for Ultrafast Imaging, University of Hamburg, Luruper Chaussee 149, 22761 Hamburg, Germany*

[5]*Department of Mathematics and Statistics, University of Massachusetts Amherst, Amherst, Massachusetts 01003, USA*

(Received 3 February 2022; accepted 6 June 2022; published 23 June 2022)

We study the existence, stability, and dynamics of vortex dipole and quadrupole configurations in the nonlinear Schrödinger (NLS) equation on the surface of a torus. For this purpose we use, in addition to the full two-dimensional NLS equation on the torus, a recently derived [N.-E. Guenther *et al.*, Phys. Rev. A **101**, 053606 (2020)] reduced point-vortex particle model which is shown to be in excellent agreement with the full NLS equation evolution. Horizontal, vertical, and diagonal stationary vortex dipoles are identified and followed, using parameter continuation, along the torus aspect ratio and the chemical potential of the solution. Windows of stability for these solutions are identified. We also investigate stationary vortex quadrupole configurations. After eliminating similar solutions induced by invariances and symmetries, we find a total of 16 distinct configurations ranging from horizontally and vertically aligned quadrupoles to rectangular and rhomboidal quadrupoles to trapezoidal and irregular quadrupoles. The stability for the least unstable and, potentially, stable quadrupole solutions is monitored at both the NLS equation and the reduced model levels. Two quadrupole configurations are found to be stable on small windows of the torus aspect ratio and a handful of quadrupoles are found to be very weakly unstable for relatively large parameter windows. Finally, we briefly study the dark-soliton stripes and their connection, through a series of bifurcation cascades, with steady-state vortex configurations.

DOI: 10.1103/PhysRevA.105.063325

I. INTRODUCTION

The study of atomic Bose-Einstein condensates (BECs) offers a pristine setting to explore the interplay of nonlinear dynamical phenomena and quantum mechanical effects [1–4]. A major thrust of associated experimental and theoretical efforts has consisted of the exploration of coherent structures supported by the interplay of effective nonlinearity and dispersion in such systems, both at the mean-field level but also beyond [5]. More specifically, relevant studies and a wide range of experiments have focused on bright solitons [6–8] in attractively interacting condensates, dark solitons in self-repulsive species [9–16], gap solitons [17], and multicomponent structures [18]. While the above have been prototypically one-dimensional states, higher-dimensional structures such as vortices [19,20] and vortex rings [21,22] have also attracted significant attention in their own right.

Naturally, this activity has been mostly focused in the prototypical settings of parabolic (but also often periodic) traps in one and higher dimensions, which have been the typical settings of experiments so far [1–3]. However, recent years have seen a surge of activity as concerns the exploration of BECs in two-dimensional (2D) surfaces. In the past year alone, multiple papers explored the dynamics of vortices and vortex-antivortex pairs in spherical surface, shell-shaped systems [23–25], following up on earlier related work not only on spherical surfaces [26], but also on cylindrical surfaces, planar annuli and sectors, and cones [27,28]. The topic of the dynamics of vortices on curved surfaces is one that bears considerable history [29] motivated by a variety of settings in fluid [30] and superfluid [31] physics. In terrestrial BEC settings, the realization of such experiments suffers from aspects such as the gravitational sag. However, the recent activity in the newly launched Cold Atomic Laboratory aboard the International Space Station seems to hold considerable promise in this direction [32–35] and indeed is specifically aiming to implement a hollow bubble geometry [36,37]. This in turn paves the way for the broader study of pattern dynamics (including topologically charged states such as vortices) in nontrivial geometry- and topology-featuring setups [23,24,27,28]. It should also be noted that this is in addition to the remarkable recent developments towards confining and manipulating atoms via adiabatic potentials, which in turn can also lead to a diverse variety of traps for ultracold atoms (see, e.g., Ref. [38] for a relevant review). It is relevant in this connection to mention that the first experiments in such bubble traps have already been reported [39]. Using a

combination of confinement techniques, such as the ones discussed above (notice in that connection that these were pioneered more than 20 years ago [40] before being brought to bear in this context), and painting optical potentials, as pioneered in the work of Ref. [41] and recently realized in microgravity settings in Ref. [34], we believe that the toroidal confinements considered herein may be within reach in the not too remote future.

In the present work, our platform of choice will be the surface a torus, i.e., the simplest compact and multiply connected surface. This is motivated by the above developments, the torus's nontrivial topological structure, the proposal by experimental groups of the realization of an optical lattice on its surface [42], and the recent formulation of the effective vortex particle dynamics on its surface [43]. More concretely, we extend our earlier considerations in the realm of bright solitary waves [44] to the self-repulsive condensate setting and the primarily vortical (but also dark-soliton stripe) set of structures that can arise therein while also respecting the periodicity of the torus in both of its angular directions. The fundamental work of Ref. [43] has set the stage by providing a description at the level of ordinary differential equations (ODEs) for the vortex particles yet has still left many questions unanswered. For instance, this description holds only for large chemical potentials such that $\{R, r\} \gg \xi$, where $\xi = 1/\sqrt{2\mu}$ is the corresponding healing length (in dimensionless units; see below for a discussion of the relevant adimensionalization). Thus, it is relevant to explore the nature of the existence, stability, and dynamics of multivortex structures as a function of the chemical potential μ (which is also a proxy for the atom number), but also as a function of the torus geometric parameters such as the ratio of the minor to the major axis. Furthermore, while the ODEs were derived, the potential equilibria of those and the associated stability and phase portraits were not explored even for the most prototypical case of a vortex pair. Indeed, there are further significant multivortex configurations that are relevant to consider such as the vortex quadrupoles. Additionally, as we will see below, the vortex patterns also bear connections (through their bifurcations) to states involving dark-solitonic stripes that are of interest in their own right. Finally, it is also particularly meaningful to compare the ODE results with direct partial differential equation (PDE) simulations to explore the validity and also potential limitations of the approach.

More concretely, our work is organized as follows. In Sec. II we introduce the original, full, spatiotemporal model on the torus and briefly review (for completeness) the main aspects of its reduction to an effective point-vortex model, as obtained in Ref. [43]. Section III presents the bulk of our results by studying the existence of vortex- and stripe-bearing solutions, their stability, and dynamics. In particular, in Sec. III A we exhaustively analyze the existence, stability, and dynamics for vortex dipole configurations. We find a total of four different stationary dipole solutions, two of which are fully stable. We also extend these solutions by adding extra phase windings along the toroidal and poloidal directions. Section III B is devoted to the study of quadrupole configurations where we identify a total of 16 distinct ones. A couple of these quadrupoles are found to be stable within small parameter windows, while a handful of quadrupoles are found to be very weakly unstable for relatively large parameter windows. In Sec. III C we briefly study the existence and stability of dark-soliton configurations and connect some of them, via bifurcation cascades, with steady-state vortex patterns. Finally, a summary and conclusions of our work, together with some possible avenues for future research, are given in Sec. IV.

II. MODEL AND THEORETICAL SETUP

A. Spatiotemporal model

As a motivation for the spatiotemporal model for a complex field on a torus, let us consider the lowest-order mean-field approximation for a dilute BEC at sufficiently low temperatures where the full 3D dynamics is well described by the Gross-Pitaevskii equation (GPE) [1–4]

$$i\hbar\psi_t = -\frac{\hbar^2}{2M}\nabla^2\psi + V_{\text{ext}}\psi + g|\psi|^2\psi. \tag{1}$$

Here $\psi(x, y, z, t)$ is the macroscopic wave function and $g = 4\pi\hbar^2 a_s/M$ is the nonlinear interaction parameter depending on the s-wave scattering length a_s and the atom mass M. The external potential $V_{\text{ext}}(x, y, z)$ holds the BEC and determines its overall shape. Specifically, considering an external trapping that confines the atoms on the surface of a torus as described in Ref. [42], the BEC wave function will be confined to a thin shell on this surface (see, for instance, Ref. [23] for a BEC confined on the surface of a sphere). Thus, similar to what is customarily done for flat pancake-shaped quasi-2D BECs [3], it is possible to average along the thin transverse direction by assuming that the chemical potential is much smaller than the energy of the first excited state along this transverse direction. Under this condition, the BEC remains in its ground state along the thin direction. This effective separation of variables results in a 2D GPE with a rescaled nonlinear interaction parameter [3] which, after appropriate rescaling of time, space, and wave function, would yield an effective 2D nonlinear Schrödinger (NLS) equation model for the BEC wave function.

Let us then consider NLS equation solutions that exist on the surface of a torus centered at the origin. The torus has a major (toroidal) radius R and a minor (poloidal) radius r such that $R > r$. The torus coordinates in 3D space are parametrized by

$$\begin{aligned} X &= [R + r\cos(\theta)]\cos(\phi), \\ Y &= [R + r\cos(\theta)]\sin(\phi), \\ Z &= r\sin(\theta). \end{aligned} \tag{2}$$

It is useful to define the angular coordinates on the torus as follows: The toroidal angle is denoted by $\phi \in [0, 2\pi]$ and poloidal angle $\theta \in [0, 2\pi]$. In particular, we choose our toroidal axis such that $\theta = 0$ corresponds to the outermost ring of the torus while $\theta = \pi$ corresponds to the innermost ring (see Fig. 1). Hence, solutions along these rings will be dubbed below as outer and inner, respectively. On the surface of this torus, in the absence of any external potentials, the 2D NLS wave function $\psi = \psi(\phi, \theta, t)$ is described by the

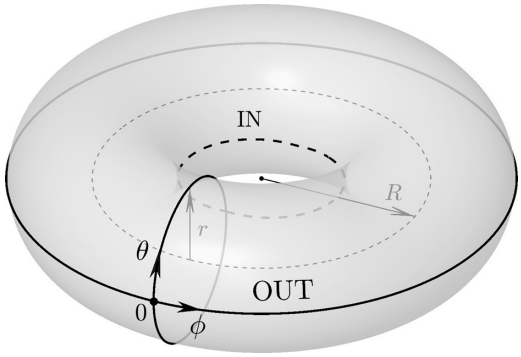

FIG. 1. Torus with major radius R and a minor radius r and the corresponding toroidal ϕ and poloidal θ angles.

adimensionalized spatiotemporal model

$$i\psi_t = -\tfrac{1}{2}\Delta\psi - \sigma|\psi|^2\psi, \tag{3}$$

where $\sigma = +1$ and -1 correspond to the focusing (attractive) and defocusing (repulsive) cases, respectively, and lengths are measured in units of $\hbar/\sqrt{Mgn_0}$, with n_0 the BEC density away from vortex cores. In the present study we exclusively examine the defocusing case that admits dark structures (i.e., structures on top of a finite background) such as dark-soliton stripes and vortices; hence, in our computations, hereafter $\sigma = -1$. Central to the description of the NLS wave function on a torus is of course the corresponding Laplace-Beltrami operator that takes the form (see, e.g., Ref. [45])

$$\Delta = \frac{1}{r^2}\frac{\partial^2}{\partial\theta^2} - \frac{\sin\theta}{r(R + r\cos\theta)}\frac{\partial}{\partial\theta} + \frac{1}{(R + r\cos\theta)^2}\frac{\partial^2}{\partial\phi^2}. \tag{4}$$

In what follows, we define the torus aspect ratio $\alpha \equiv r/R$.

B. Steady states and stability

In Sec. III we will construct and study several steady-state solutions for the above NLS equation on the torus. These steady states (standing waves) are found by separating space and time variables according to $\psi(\phi, \theta, t) = \varphi_0(\phi, \theta)\, e^{-i\mu t}$, where μ is often referred to as the chemical potential and corresponds to the temporal frequency of the solution (as well as to the density of its background). Thus, the steady-state NLS equation for $\varphi_0(\phi, \theta)$, parametrized by μ, reads

$$-\tfrac{1}{2}\Delta\varphi_0 - \sigma|\varphi_0|^2\varphi_0 - \mu\varphi_0 = 0. \tag{5}$$

After suitably identifying steady states (for numerical details, see below), it is relevant to study their dynamical stability properties by extracting the corresponding stability spectra. Therefore, we follow perturbed solutions starting by a steady state φ_0 as per Eq. (5) and perturbing it with an infinitesimal perturbation according to

$$\psi = \{\varphi_0 + \varepsilon[ae^{\lambda t} + b^* e^{\lambda^* t}]\}e^{-i\mu t}, \tag{6}$$

where $a = a(\phi, \theta)$ and $b = b(\phi, \theta)$ correspond to the spatial eigenmodes with eigenvalue λ. Then the so-called Bogoliubov–de Gennes (BdG) stability spectrum is obtained by solving the linearized equation (i.e., to order ε^1)

$$\begin{bmatrix} M_1 & M_2 \\ -M_2^* & -M_1 \end{bmatrix}\begin{bmatrix} a \\ b \end{bmatrix} = -i\lambda\begin{bmatrix} a \\ b \end{bmatrix}, \tag{7}$$

where $M_1 = \frac{1}{2}\Delta + \mu + 2\sigma|\varphi_0|^2$ and $M_2 = \sigma\varphi_0^2$. By construction, the spectrum obtained from Eq. (6) will respect the Hamiltonian symmetry such that if λ is an eigenvalue, so are $-\lambda$, λ^*, and $-\lambda^*$, where the asterisk stands for complex conjugation. Therefore, any eigenvalue such that $\mathrm{Re}(\lambda) > 0$ will correspond to an instability: an exponential instability if $\mathrm{Im}(\lambda) = 0$ and an oscillatory instability if $\mathrm{Im}(\lambda) \neq 0$. In the latter case, the exponential growth is also accompanied by an oscillatory dynamics of the solution.

In the present work we focus primarily on stationary solutions composed of multivortex configurations. Similar to the focusing case of Ref. [44], there will be special vortex locations on the torus corresponding to stationary configurations. It is important to mention that, due to the periodic nature of the domain, only configurations with zero total charge are allowed. Therefore, only configurations with the same number of positively and negatively charge vortices are possible within the toroidal geometry. Therefore, we will focus on the lowest-order ones that correspond to vortex dipoles and quadrupoles. As indicated also in the Introduction, even for the former there are many important features to explore including their stationary configurations and associated stability. The periodicity of the domain also allows for the existence of dark-soliton-stripe configurations provided they appear in pairs to allow for the individual π phase jumps of each dark soliton to accumulate to a whole 2π phase jump. Nonetheless, as we will see in Sec. III C, configurations with an odd number of dark-soliton stripes are also possible by adding extra phase windings (perpendicular to the stripes) to respect the periodicity. Finally, it is also relevant to note that the Laplacian operator in Eq. (4) is translationally invariant along the toroidal ϕ direction. Thus, steady-state solutions will generate an entire family of possible ϕ translates, unless the steady state is already homogeneous in the ϕ direction such as all horizontal (toroidal) dark-soliton-stripe configurations.

C. Reduced point-vortex particle model

In tandem with the procurement of steady states and their characterization (stability), we will study the corresponding elements in the dynamically reduced model where the vortices are considered as point particles, as per the fundamental work of Ref. [43]. Note that, in comparison to the latter, we are using here adimensional variables which correspond to the models in these works with $\hbar = M = 1$, where M is the mass of the particles forming the atomic BEC. The model is cast as a set of ODEs on the vortex positions. This point-vortex model assumes that the vortices possess a quantized vorticity, that they have no internal (density) structure, and that the only effects come from vortex-vortex phase interactions and, importantly, the curvature effects from the toroidal substrate where they are embedded. Such point-vortex models have been shown to be accurate in the (sufficiently) large-μ limit [3,19]. Indeed, what we will conclude here as well is that when the width of the vortex cores, given by the healing length $\xi = 1/\sqrt{2\mu}$, is sufficiently small compared to the torus

circumferences $2\pi r$ and $2\pi R$, the reduced model gives an accurate static (steady states), stability, and dynamical representation of the full NLS equation model on a torus. In fact, as we will see in Sec. III, even for relatively small values of α around 0.15 with $R = 12$, corresponding to a small circumference of the torus of $r = 0.15 \times 12 < 2$, the effective ODE for $\mu = 1$, corresponding to a healing length of $\xi = 1/\sqrt{2} \simeq 0.7$, still gives an accurate (qualitative and quantitative) description of the original full NLS equation model.

In the large-μ limit, one only considers the phase of the vortices and how the superposition of the phases from all other vortices advects the position of each vortex through the identification of the local fluid velocity as the gradient of the wave function's phase at that point. The key toward setting up the point-vortex model on the torus lies in taking into consideration two crucial effects that are absent in the standard NLS equation model on a flat and infinite domain, namely, (i) the effects of the periodic boundary conditions and (ii) the effects of the torus's curvature. The periodic boundary conditions are accounted for by placing "ghost" (or mirror) vortices outside the domain accounting for the effects that a particular vortex has on itself through the boundaries as well as the effects of the other vortices through the boundaries. This cumulative process results in an infinite sum for these contributions that can be represented in the form of Weierstrass functions or in terms of Jacobi-θ functions (see Ref. [46] and references therein). On the other hand, the effect of curvature from the torus can be more conveniently captured by expressing the system in isothermal coordinates. Following Ref. [43], one defines the isothermal coordinates (u, v) related to the toroidal (ϕ, θ) ones through [47]

$$\phi = \frac{u}{c}, \quad \theta = 2\tan^{-1}\left[\sqrt{\frac{R+r}{R-r}}\tan\left(\frac{v}{2r}\right)\right], \tag{8}$$

where $c \equiv \sqrt{R^2 - r^2}$. Then it is possible to show that these new (u, v) coordinates, with squared line element $ds^2 = \Lambda^2(du^2 + dv^2)$, are indeed isothermal (i.e., local ones in which the metric is conformal to the Euclidean) where the local scale factor satisfies

$$\Lambda = \frac{c}{R - r\cos(v/r)}. \tag{9}$$

Note that the scale factor only depends on the poloidal location, namely, $\Lambda = \Lambda(v)$, since the system is translationally invariant along the toroidal direction. The isothermal coordinates (u, v) are then defined on the periodic rectangle $[-\pi c, \pi c] \times [-\pi r, \pi r]$.

Taking the periodic and curvature effects and defining the complex coordinate $w = u + iv$, the work of Ref. [43] gives the explicit form for the wave function's phase Φ associated with a set of vortex dipoles composed of a total zero charge configuration of vortices with charges q_n at (isothermal) positions w_n, namely, $\Phi(w) = \mathrm{Im}[\mathcal{F}(w)]$, where $\mathcal{F}(w) = \sum_n q_n F(w, w_n)$, with

$$F(w, w_n) \equiv \ln\left[\vartheta_1\left(\frac{w - w_n}{2c}, p\right)\right] - \frac{\mathrm{Re}(w_n)}{2\pi rc}w, \tag{10}$$

where $\vartheta_1(w, p)$ is the first Jacobi-θ function evaluated at w with nome $p \equiv e^{-\pi r/c}$ $(0 < p < 1)$. The first Jacobi-θ function may be written as the infinite sum

$$\vartheta_1(w, p) = 2p^{1/4}\sum_{n=0}^{\infty}(-1)^n p^{n(n+1)}\sin[(2n+1)w]. \tag{11}$$

Note that this implementation of ϑ_1 requires, for typical numerical values used in this paper, less than a dozen terms for this infinite sum to converge to machine (double) precision. From this overall phase imparted by all the vortex dipoles, one can explicitly write equations of motion for the individual vortices through the fluid velocity that in turn is equivalent to the gradient of the phase. Thus, the nth vortex will experience a velocity V_n given by the gradient of the phase imprinted by the *other* vortices. Expressing the velocity in complex coordinates $V_n = \dot{u}_n + i\dot{v}_n$ yields $\dot{u}_n = \mathrm{Im}(\Omega_n)/\Lambda(v_n)$ and $\dot{v}_n = \mathrm{Re}(\Omega_n)/\Lambda(v_n)$, where

$$\Omega_n = \frac{1}{\Lambda(v_n)}\left[\sum_{m\neq n} q_m f(w_n, w_m) + i\frac{q_n}{2}\frac{\Lambda'(v_n)}{\Lambda(v_n)} - \frac{q_n u_n}{2\pi rc}\right], \tag{12}$$

where

$$f(w, w_n) \equiv \partial_w F(w, w_n). \tag{13}$$

Note that the sum excludes self-interacting terms (i.e., $m \neq n$). The three contributions in Eq. (12) correspond, respectively, to (i) the classical vortex-vortex logarithmic-potential interactions, (ii) the effects of curvature of the torus on each vortex, and (iii) the correction to the velocity to satisfy periodicity along the torus, which imposes the quantization of flow along the torus. By construction, the function $f(w, w_n)$ is periodic in both the imaginary (vertical) and real (horizontal) directions. The vertical periodicity is captured from the explicit periodicity of the Jacobi-θ function itself, while the horizontal periodicity is achieved by judiciously adding a linear term in the horizontal direction [see the last term in Eq. (10)], which ensures continuity of the velocity in the periodic domain [43]. In the next section, the point-vortex model, cast through the explicit velocity formulation of Eq. (12), is validated against numerical results from the full NLS equation (3). This point-vortex model will also be instrumental in finding stationary dipole and quadrupole solutions.

III. NUMERICAL RESULTS

In order to find branches of solutions as the system parameters are varied it is usually sufficient to find a single element of the branch and then apply numerical continuation to extend each branch over these parameters and study their existence and stability as the system parameters (mostly the chemical potential μ and the torus aspect ratio α) are varied. Thus, let us now leverage the results from the preceding section to find particular stationary vortex configurations (dipoles and quadrupoles) for the reduced ODE model (12) and from there construct approximate steady states for the full NLS equation (3) that can be used with a fixed-point iteration scheme (cf. Newton's method) to find numerically exact steady states. Once a particular steady state of (even) N vortices with charges q_n and locations (u_n, v_n) is identified in the reduced ODE model, we construct an approximate initial wave-function seed φ_0 by "superimposing" individual

vortexlike guesses as

$$\varphi_0(u,v) = \sqrt{\mu} e^{i\Phi(u,v)} \prod_{n=1}^{N} A(u-u_n, v-v_n), \tag{14}$$

containing the following ingredients. (i) The background level is fixed so that, away from vortices, the density $|\varphi_0|^2$ tends to μ. (ii) The global phase $\Phi(u,v)$ is prescribed by the ODE model as per $\Phi(w) = \mathrm{Im}[\sum_n q_n F(w, w_n)]$, with F defined in Eq. (10). (iii) Each vortex (absolute value) profile is approximated by

$$A(u,v) = \tanh(\sqrt{\mu}\sqrt{u^2+v^2}), \tag{15}$$

centered at each of the vortex locations (u_n, v_n). In a similar vein, one can also construct approximate dark-soliton-stripe solutions as

$$\varphi_0(u,v) = \sqrt{\mu} \prod_{n=1}^{N} B(u_n, v_n), \tag{16}$$

where $B(u_n, v_n) = A(u-u_n, 0)$ for dark stripes aligned along the poloidal direction and $B(u_n, v_n) = A(0, v-v_n)$ for dark stripes aligned along the toroidal direction. After a particular initial seed is constructed in the isothermal coordinates, it is converted to toroidal coordinates (ϕ, θ) as per the transformation (8) or to Cartesian coordinates $(x, y) = (R\phi, r\theta)$ on the surface of the torus. Note that, as per Eq. (2), (X, Y, Z) describes the Cartesian coordinates for a point on the torus in 3D space while (x, y) describes the Cartesian 2D coordinates on the *surface* of the torus. Steady states are then found using Newton's method by discretizing space using second-order central finite differences (FDs) and separating real and imaginary parts. We use a 2D grid of $N_\phi \times N_\theta$ mesh points to discretize the wave function giving rise to a Newton matrix of size $2N_\phi N_\theta \times 2N_\phi N_\theta$. In our numerics below we typically use $N_\phi = N_\theta = 490$. Similarly, for the numerical stability results, we use the same FD discretization in space to cast the eigenvalue-eigenfunction problem (7) as a standard eigenvalue-eigenvector problem for the resulting stability matrix of size $2N_\phi^2 N_\theta^2 \times 2N_\phi^2 N_\theta^2$. Finally, for the numerical integration of the full NLS equation (3), we use again the same FD discretization in space and a standard fourth-order Runge-Kutta method in time.

A. Vortex dipoles

1. Steady states

Through the reduced ODE model, one can browse the entire phase space of solutions for vortex dipoles given by a $+1$ vortex at location (ϕ_1, θ_1) and a -1 vortex at (ϕ_2, θ_2). Since the system is translationally invariant in the toroidal direction, the original phase space $(\phi_1, \theta_1, \phi_2, \theta_2)$ can be reduced, without loss of generality, to $(\bar{\phi}, \theta_1, -\bar{\phi}, \theta_2)$ by centering the solution about the toroidal axis with $\bar{\phi} = (\phi_1 + \phi_2)/2$. A numerically exhaustive search for steady states in the three-dimensional reduced space $(\bar{\phi}, \theta_1, \theta_2)$, using a standard fixed-point iteration method (nonlinear least squares with a Levenberg-Marquardt algorithm), is then straightforward and yields four different types of stationary dipoles.

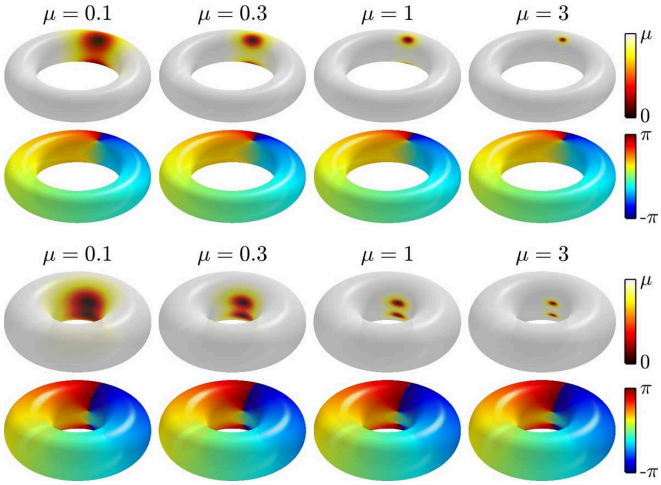

FIG. 2. Steady-state solutions continued from the vertical dipole-in configuration. The modulus squared (top) and the phase (bottom) of the solutions are plotted on the surface of the torus. The different solutions correspond to the values of μ indicated in the panels and $R = 12$ while $\alpha = 0.4$ for the top group of panels and $\alpha = 0.7$ for the bottom group of panels.

(i) Vertical dipole-in configuration. This solution corresponds to a vertically (poloidally) aligned dipole with $\phi_1 = \phi_2$ and $\theta_1 = -\theta_2$. We dub this solution to be "in" as the value of $|\theta_1| = |\theta_2|$ is closer to $\theta = \pi$, the inner part of the torus, than to the outer part with $\theta = 0$. Figure 2 depicts several steady-state solutions continued from the vertical dipole for $R = 12$, a couple of values of α, and different values of μ.

(ii) Horizontal dipole-in configuration. This solution corresponds to a horizontally (toroidally) aligned dipole with $\theta_1 = \theta_2 = \pi$, i.e., on the inside of the torus (see Fig. 3).

(iii) Horizontal dipole-out configuration. This solution corresponds to a horizontally (toroidally) aligned dipole with $\theta_1 = \theta_2 = 0$, i.e., on the outside of the torus (see Fig. 4).

(iv) Diagonal dipole configuration. This solution corresponds to a diagonal dipole with $(\phi_2, \theta_2) = -(\phi_1, \theta_1)$ owing

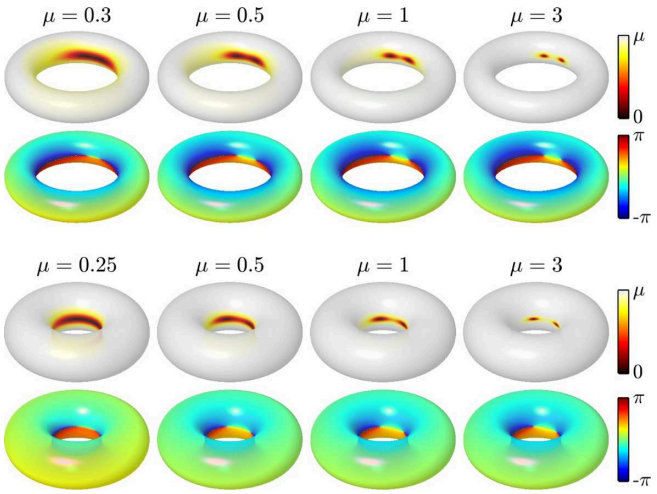

FIG. 3. Steady-state solutions continued from the horizontal dipole-in configuration. The layout and parameters are the same as in Fig. 2.

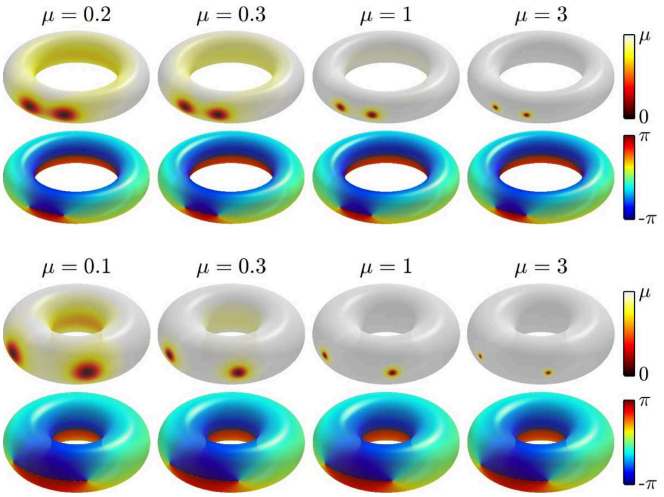

FIG. 4. Steady-state solutions continued from the horizontal dipole-out configuration. The layout and parameters are the same as in Fig. 2.

to a nontrivial balance of all the vortex velocity components (see Fig. 5). This is arguably the least intuitively expected among the different solutions.

At an intuitive level, one can argue that the main phenomenology involves a combination of different factors. On the one hand, a well-known fact stemming from their nonlinear phase-induced interaction is that two vortices in Euclidean space will travel parallel to each other (in a direction perpendicular to their line of sight). The curvature arising from the toroidal geometry leads to that feature being modified. However, it is interesting to note that, along the torus equators ($\theta = 0$ and $\theta = \pi$), the horizontal (out and in) dipoles will interact with each other by exerting mutual velocities that are purely poloidal and that, on the other hand, vertical dipoles that are symmetric with respect to $\theta = 0$ will only experience mutual interactions with purely toroidal velocities. On the other hand, the topology of the torus and its periodic boundary

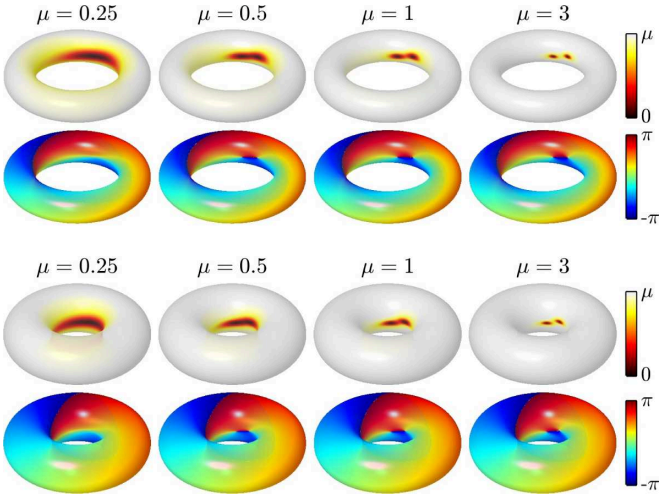

FIG. 5. Steady-state solutions continued from the diagonal dipole configuration. The layout and parameters are the same as in Fig. 2.

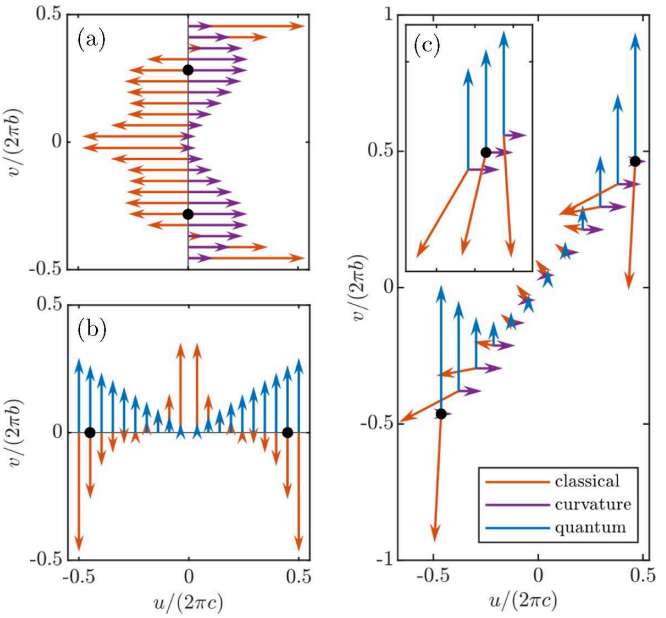

FIG. 6. Velocity fields for (a) the vertical dipole-in configuration, (b) the horizontal dipole-out configuration, and (c) the diagonal dipole configuration for $\alpha = 0.5$. The different contributions to the velocity are as follows: red arrows, classical vortex-vortex interactions; purple arrows, effects of curvature on each vortex; and blue arrows, quantum correction to ensure periodicity on the torus. The black dots depict the locations of the vortices that balance all the velocity contributions and give rise to steady-state configurations. Note that we do not present the plot of the horizontal dipole-in configuration as its velocity field is qualitatively the same as for the horizontal dipole-out configuration but just shifted in the poloidal direction to $\theta = \pi$. Also depicted in (c) is a close-up of the (scaled) velocity fields close to the steady-state configuration showing a perfect balance of the three velocity contributions giving rise to a nontrivial diagonal dipole steady-state configuration.

conditions come into play and effectively create an equal and opposite velocity at these suitably selected distances, creating the potential for the steady states that we consider herein. More specifically, Fig. 6 depicts the different contributions to the velocities of vortex dipoles that support steady-state configurations. For instance, it is straightforward to conclude that any initial condition corresponding to a symmetric ($u_1 = u_2$ and $v_1 = -v_2$) vertical dipole will always remain a symmetric vertical dipole with a constant separation (this is in tune with the translational invariance along the toroidal direction). Also, a horizontal dipole will always remain a horizontal dipole as the toroidal contributions to each vortex are equal.

Furthermore, as depicted in Fig. 6, there is a specific location (depending on the parameters of the system) for the vertical dipole that leads to a perfect balance of all the velocity contributions giving rise to a steady-state configuration. Figure 6(a) shows the velocity contributions to the vortices where the curvature effects (purple arrows) always point to the right while the vortex-vortex interactions (red arrows) point to the right if the vortices are closer to the inside of the torus and point to the left if they are closer to the outside of the torus. As a result, it is possible to find a steady-state vertical configuration that balances these two effects (see black

dots). On the other hand, horizontal dipoles do not exhibit contributions to velocity coming from curvature effects when exactly placed in the outside ($\theta = 0$) or outside ($\theta = \pi$) of the torus. However, as can be seen in Fig. 6(b), in addition to the vortex-vortex interactions (see red arrows), horizontal dipoles do experience a toroidal contribution to the velocity due to the quantum term in the equations of motion (see blue arrows). As for the vertical dipole, the direction of the vortex-vortex interactions can change sign depending on whether the two vortices get closer on one side or the other of the torus while the velocity due to the quantum term always points upward. As a result, it is also possible to find a steady-state horizontal configuration that balances these two effects (see black dots). The phenomenology is exactly the same for the horizontal dipole-in and dipole-out configurations with curvature contributions being absent for both. Finally, as Fig. 6(c) shows, there is a nontrivial solution where the three contributions to the velocity are nonzero and yet they perfectly balance each other, giving rise to a diagonal dipole steady-state configuration.

Returning to the vertical steady-state dipole, this solution exists as there is no poloidal contribution to the vortex velocities and the toroidal contribution from curvature balances the vortex-vortex contribution (also toroidal). In fact, the velocity balancing argument suggests that, for each value of α, there seems to be a single vertical dipole distance that leads to a steady state. The figure also suggests that the steady-state vertical dipole is always *unstable* as, e.g., perturbations along the poloidal direction will naturally result in (i) a constant toroidal velocity of the dipole if the vortex perturbations are equal and opposite in the poloidal direction and, for generic perturbations, (ii) a toroidal velocity imbalance will start deviating from the stationary state. This instability of the vertical dipole-in configuration will be revisited, for both PDE and ODE models, in Sec. III A 3.

On the other hand, as depicted in Fig. 7, it is possible to reduce the phase space for horizontal dipoles to two dimensions since, as mentioned above, a horizontal dipole will stay horizontal for all times. The figure suggests that there exist two horizontal dipoles as we described above: one at $\theta = 0$ (horizontal dipole-out configuration, denoted by black dots in the figure) and one at $\theta = \pi$ (horizontal dipole-in configuration, denoted by black pluses). Furthermore, the figure suggests that the horizontal dipole-out configuration is (neutrally) stable as a center within the relevant phase portrait, while the horizontal dipole-in configuration is unstable (i.e., a saddle point). A full explanation of the results for the phase space of vertical dipoles is given below in Sec. III A 4. Furthermore, for all steady-state dipole configurations, their stability will be covered, for both PDE and ODE models, in Sec. III A 3.

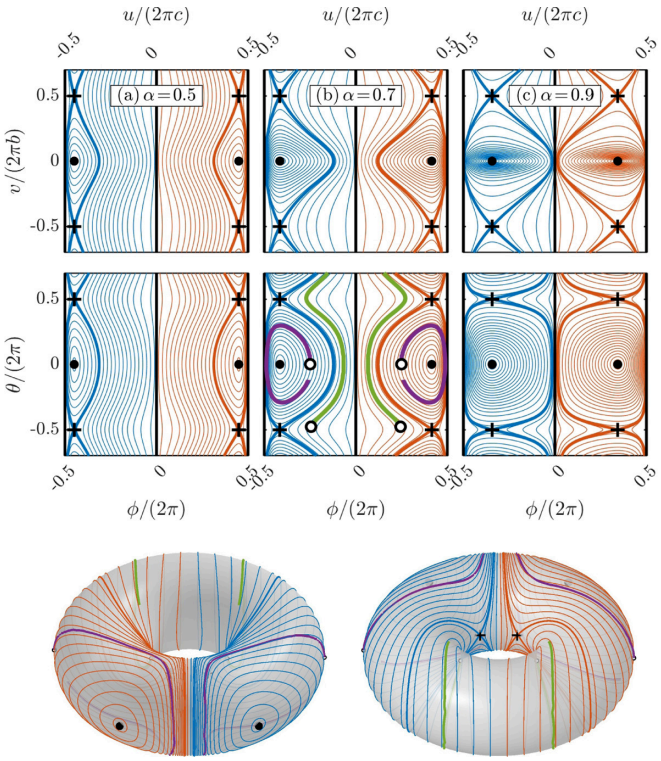

FIG. 7. Planar phase space for symmetric horizontal dipole configurations. The top and middle rows depict isothermal and toroidal coordinates, respectively, and the different columns correspond to the indicated values for α. The bottom row depicts the front (left) and back (right) views of the $\alpha = 0.7$ case projected on the surface of the torus. The different orbits are generated from initial conditions corresponding to symmetric perturbations from the (neutrally) stable horizontal dipole-out configuration (black dots). The separatrices (thick curves) correspond to the stable and unstable manifolds of the horizontal dipole-in configuration (black pluses). The separatrices divide the phase space in areas containing oscillating orbits and rotating (wrapping poloidally) orbits. For $\alpha = 0.7$ we also depict the trajectories from full PDE simulations for $\mu = 1$ corresponding to an oscillating orbit (thick purple line) and a rotating one (thick green line) starting at the initial positions depicted by the corresponding white dots that are located at the outer ($\theta = 0$) and inner ($\theta = \pi$) parts of the torus, respectively.

2. *Quantized flow currents: Phase windings*

By following the construction of steady-state vertical dipoles as per Fig. 6, it is apparent that there is no vertical dipole that could be dubbed "out." This fact can be rationalized by noting that the velocity contribution from curvature close to $\theta = 0$ (i.e., on the outer part of the torus) is very weak and cannot counter the (stronger) velocity contribution from the vortex-vortex interaction. Nonetheless, let us note that it is possible, in the NLS equation model, to add extra phase windings along the toroidal and poloidal directions provided one respects the periodicity of the domain. In fact, any NLS configuration $\psi(\phi, \theta)$ can always be multiplied by a phase term with W_x bearing an extra 2π winding in the toroidal direction and W_y an extra 2π winding in the poloidal direction without violating the periodicity of the domain. These extra phase windings physically correspond to adding rotations along the toroidal and poloidal directions with quantized speeds. Thus, inspired by the vertical and horizontal dipoles described above, one can take each of these solutions and multiply them by a phase term as

$$\psi(\phi, \theta) \to \psi(\phi, \theta) e^{iW_x \phi} e^{iW_y \theta}, \tag{17}$$

where the windings W_x and W_y are integers. In a sense these structures bear two sets of topological charges, with one

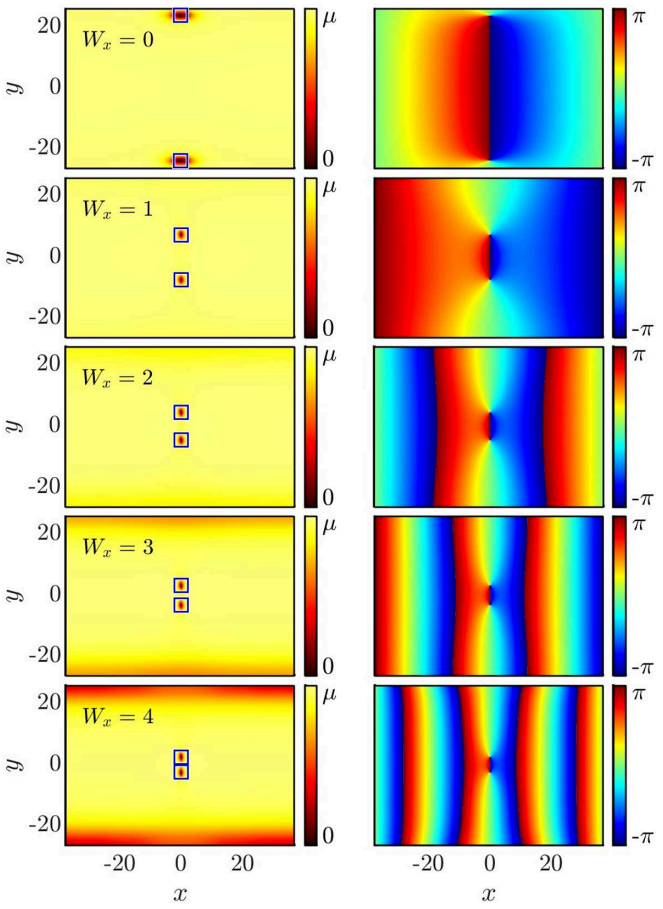

FIG. 8. Stationary vertical dipole solutions with increasing horizontal windings W_x (and $W_y = 0$) for $\alpha = 0.7$, $\mu = 1$, and $R = 12$. The left and right columns depict the density and phase of the solutions in Cartesian coordinates, respectively. The location of the vortices corresponding to the ODE model is overlaid on the density plot using blue squares. The top row corresponds to the standard vertical dipole-in configuration without extra winding ($W_x = 0$) and each successive row corresponds to a stationary vertical dipole solution with increasing horizontal winding number W_x, with the vortices getting closer to compensate for the additional speed in the opposite direction provided by the winding.

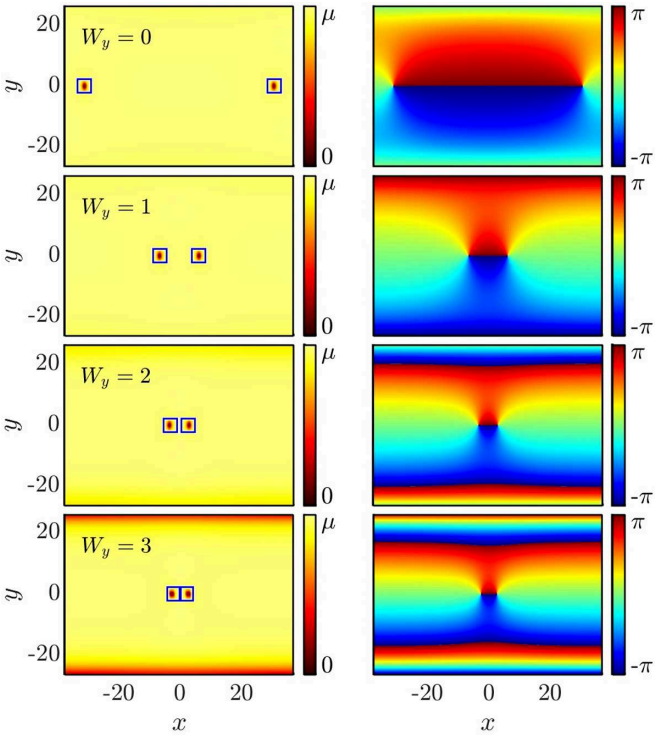

FIG. 9. Same as Fig. 8 but for stationary horizontal dipoles for $\alpha = 0.7$, $\mu = 1$, and $R = 12$ with vertical windings W_y (and $W_x = 0$).

stemming from the charge of the vortex constituents, while the second arises through the potential windings along the toroidal or poloidal (or both) directions around the torus. These phase windings ultimately correspond to including additional quantized flow currents along these directions.

It is important to note that the configurations described above, obtained from the additional phase windings described in Eq. (17), will *not* directly yield steady-state solutions of the NLS equation. However, they serve as a motivation to search for such winding-bearing steady states. Using this idea, we took the vertical dipole-in and horizontal dipole-out steady-state configurations and progressively applied, respectively, horizontal and vertical windings in tandem with the fixed point iteration scheme (Newton) to obtain families of dipoles with higher windings. We showcase examples of higher-winding vertical and horizontal dipoles in Figs. 8 and 9, respectively. It is interesting to note that the vertical dipole steady state with $W_x \geqslant 1$ gives rise to vertical dipoles that could be dubbed out as, in order to balance the extra vertical winding the vortices have to get close to each other around $\theta = 0$.

It is possible to leverage the reduced equations of motion to include the effects of vertical and horizontal windings [43]. This relies on assuming that both toroidal and poloidal contributions to the phase windings in isothermal coordinates are accounted for by *linear* phase gradients. Under this assumption, we incorporate linear phase windings that gain $2\pi W_x$ and $2\pi W_y$ along the horizontal and vertical directions, respectively. These windings are captured by adding corresponding linear terms in Ω_n of Eq. (12) as follows:

$$\Omega_n \to \Omega_n + \frac{1}{\Lambda(v_n)}\left[i\frac{W_x}{c} + \frac{W_y}{r}\right]. \tag{18}$$

The corresponding fixed points obtained from this extended reduced model with vertical and horizontal windings are depicted by the blue squares in the different panels of Figs. 8 and 9, respectively. As evidenced from these figures, this extended reduced ODE accurately predicts the stationary locations of vortex dipole configurations including vertical and horizontal windings. Furthermore, as we will see in the next section, this extended reduced ODE will also accurately describe the stability properties of these stationary dipole configurations.

3. *Stability*

Equipped with the steady-state dipole solutions described in the previous sections, let us now study their stability

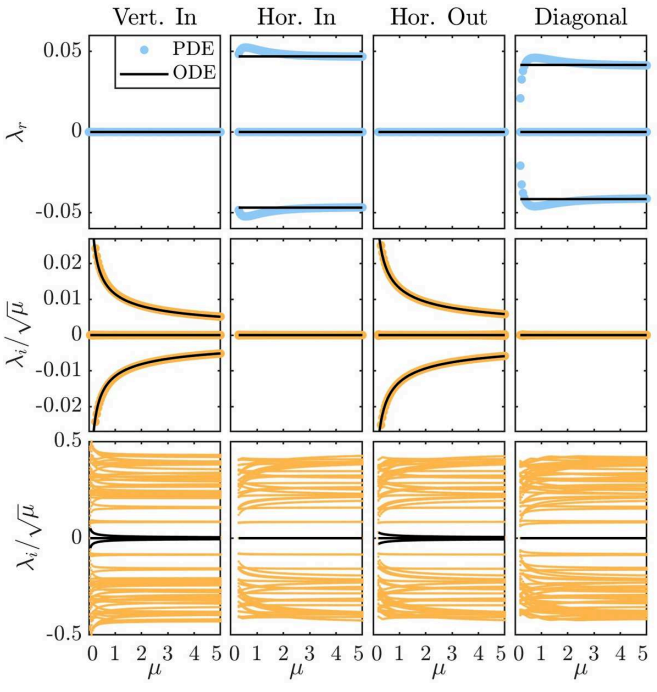

FIG. 10. Convergence of the stability spectrum for dipole configurations as the chemical potential μ is increased for $\alpha = 0.4$ and $R = 12$. The columns correspond, from left to right, to the vertical dipole-in, horizontal dipole-in, horizontal dipole-out, and diagonal dipole configurations. The top row depicts the real part of the linearization eigenvalues λ_r where the large (light blue) dots correspond to the full BdG spectra computation of the PDE while the black solid line depicts the corresponding results from the reduced ODE model. Note that $\lambda_r > 0$ is associated with an unstable solution. The middle and bottom rows depict the imaginary part of the linearization eigenvalues λ_i (normalized by $\sqrt{\mu}$) where again the large (orange) dots correspond to the PDE while the black solid line corresponds to the ODE. The middle row is a zoomed-in version of the bottom row.

properties at the full NLS equation and reduced ODE levels. Figure 10 depicts the stability spectra for the four dipole solutions in both the full NLS equation model (large colored dots) and the reduced ODE model (black curves) as μ is varied. We note that the stability eigenvalues $\lambda = \lambda_r + i\lambda_i$ determine the stability of the corresponding solutions as follows: (i) $\lambda_r = 0$ corresponds to a (neutrally) stable solution, (ii) $\lambda_r \neq 0$ and $\lambda_i = 0$ correspond to an exponential instability, and (iii) $\lambda_r \neq 0$ and $\lambda_i \neq 0$ correspond to an oscillatory instability. As Fig. 10 indicates, for the parameters used (namely, $\alpha = 0.4$ and $R = 12$), the vertical and horizontal dipole-out configurations are stable, while the horizontal and diagonal dipole-in configurations are unstable. Importantly, the figure also evidences the striking match of the reduced ODE model and the PDE findings, with the former very accurately capturing the eigenvalues associated with the motion of the vortices. Recall that the reduced ODE model is predicated on the condition of the vortices representing a point particle. This is certainly true in the large-μ limit where the size of the vortex cores (tantamount to the healing length proportional to $1/\sqrt{2\mu}$) tends to zero. However, even for relatively small values of μ, the particle model prediction for the eigenvalues remains remarkably accurate. Indeed, even moderate values of $\mu \gtrsim 3$ converge such that the relative errors for λ_r and λ_i are always less than 1%. However, it is important to mention that configurations bearing vortices that are closer than a few times their width will not be accurately captured by the reduced ODE. In fact, extreme cases could lead to the annihilation of oppositely charged vortices in the full NLS equation, while such a scenario does not arise in the reduced ODE model that considers the vortices as point particles (with zero width).

Let us now study the bifurcation scenarios when the aspect ratio α of the torus is varied. This nontrivial effect changes in a nonlinear fashion the relative size of the vortex-vortex contributions and the curvature effects and thus one could expect interesting bifurcations. Figures 11 and 12 depict the stability eigenvalues (alongside typical solutions) for the constant background state and the four possible dipole configurations (with $W_x = W_y = 0$, namely, without any extra windings) for $\mu = 1$ and $\mu = 5$, respectively. The spectrum for the constant background is supplied in the figures so that one is able to identify the eigenvalues that come from the actual vortices and those that stem from the background where they are embedded. Naturally, the ODE model is only able to capture the former set of eigenvalues originating exclusively from the relative motion of the vortices. As before, we note that the reduced ODE model reproduces remarkably well the relevant eigenvalues. In particular, for $\mu = 5$ the match between the NLS equation and reduced ODE spectrum is striking, although it should be noted that the relevant match is fairly reasonable even for $\mu = 1$. In fact, the reduced ODE is able to perfectly capture (qualitatively and quantitatively) the bifurcation suffered by the diagonal dipole where it is rendered stable for $\alpha \gtrsim 0.71$ (for $\mu = 5$). For the other solutions, as it was shown in Fig. 10, the spectra for different torus aspect ratios α of Figs. 11 and 12 tend to indicate that the vertical dipole-in and horizontal dipole-out configurations are stable while the horizontal dipole-in and diagonal dipole configurations are unstable. In each case, the effective particle equations bear a vanishing eigenvalue associated with the neutrality of the relevant solutions against shifts along the toroidal direction ϕ. It is thus only the remaining pair of eigenvalues and the pertinent "internal mode" of the dipole dynamical motion that is responsible for the stability (in the case of the vertical dipole-in and horizontal dipole-out configurations) and for the instability (for the remaining horizontal dipole-in and diagonal cases).

To complement the stability results, we include in Fig. 13 the stability spectra of the vertical dipole solution alongside their corresponding dipoles with a winding $W_x = 1$. As the figure suggests, adding a winding completely changes the stability picture by destabilizing the vertical dipole solution. This is in line with the general expectation that higher winding wave patterns are less likely to be dynamically robust than lower winding ones. Furthermore, we again obtain remarkable agreement of the stability spectrum results between the full NLS equation and, in this case, the extended reduced ODE model (18) including vertical and horizontal windings. Further studies on solutions bearing windings, including mixed combinations of vertical and horizontal windings, at the NLS

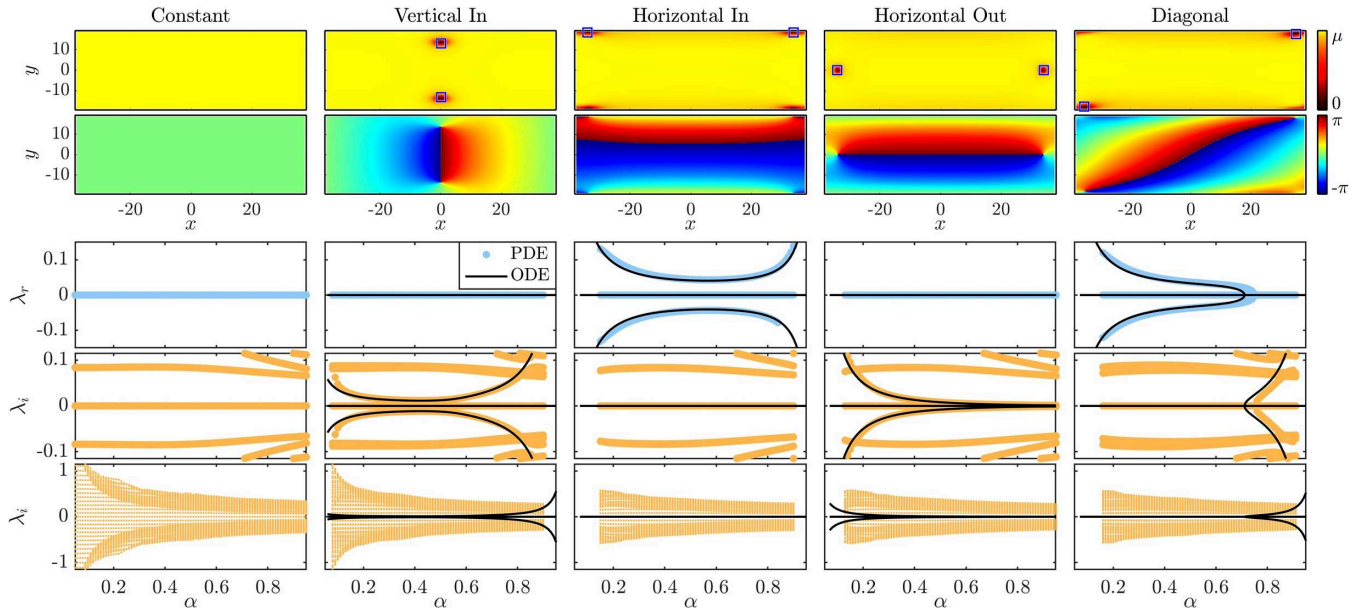

FIG. 11. Stability for dipole configurations as α is varied for $\mu = 1$ and $R = 12$. The columns correspond, from left to right, to the constant, vertical dipole-in, horizontal dipole-in, horizontal dipole-out, and diagonal dipole configurations. The top two rows depict the density and phase of the steady-state PDE solution for $\alpha = 0.5$ in Cartesian coordinates, respectively. The location of the vortices corresponding to the ODE model are overlaid on the density plot using blue squares. The third row depicts the real part of the linearization eigenvalues λ_r where the large (light blue) dots correspond to the full BdG spectra computation of the PDE while the black solid line depicts the corresponding results from the ODE model. The bottom two rows depict the imaginary part of the stability eigenvalues λ_i where again the large (orange) dots correspond to the PDE while the black solid line corresponds to the ODE. The fourth row of panels is a zoomed-in version of the bottom row.

equation and ODE levels are outside the scope of the present work and are thus left for future explorations.

4. Dynamics

In this section we present some results pertaining the dynamics of vortex dipole configurations. For instance, Fig. 7 depicts the dynamics for horizontal dipoles from the reduced ODE model. Interestingly, the stable and unstable manifolds of the unstable (saddle) horizontal dipole-in configuration coincide in a homoclinic orbit and define a separatrix between oscillating (librating) solutions around the horizontal dipole-out and rotating solutions that wrap along the poloidal direction. In the case of $\alpha = 0.7$ we also include two NLS

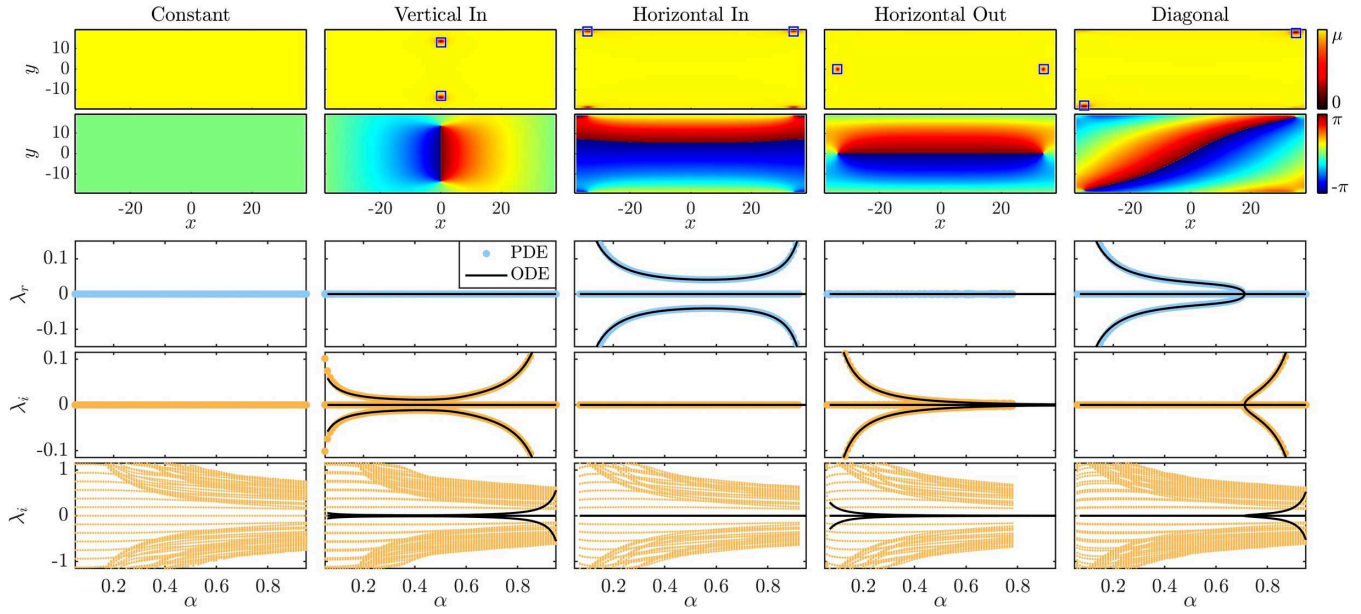

FIG. 12. Same as Fig. 11 but for $\mu = 5$. Notice the better match between the PDE and ODE results as the latter is obtained for the point-vortex model in the large-μ limit.

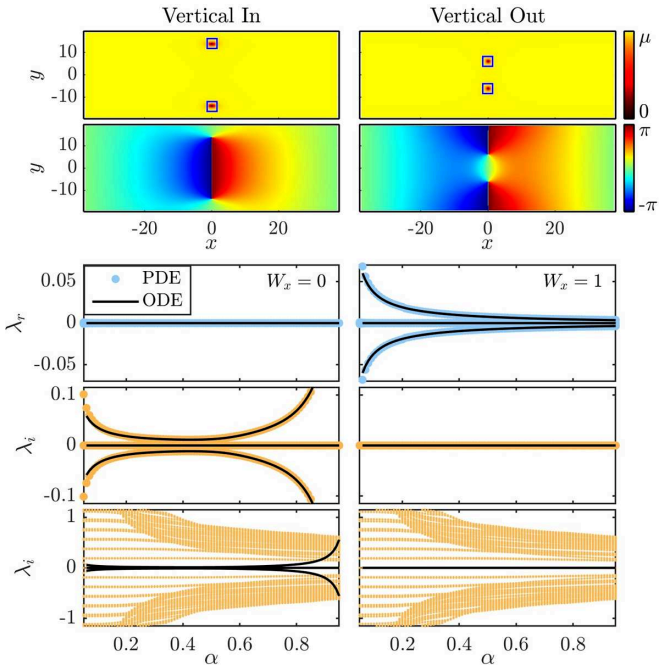

FIG. 13. Stability spectra vs α for the stationary vertical dipoles without any winding ($W_x = 0$, left panels) and with one horizontal winding ($W_x = 1$, right panels) for $R = 12$ and $\mu = 5$ (see top two rows of Fig. 8). The layout and parameters are the same as in Fig. 12. Note that the addition of a horizontal winding destabilizes the vertical dipole.

orbits obtained from initial positions as indicated in the figure and a phase profile given, as before, by $\Phi(w) = \mathrm{Im}[\sum_n q_n F(w, w_n)]$. The NLS orbits were extracted by doing a local fit of the extrema of the vorticity, defined as the curl of the velocity, with the latter defined as is standard in NLS settings [3], i.e.,

$$\mathcal{V} = -\frac{i}{2}\frac{\psi^*\nabla\psi - \psi\nabla\psi^*}{|\psi|^2}. \tag{19}$$

The purple and green NLS orbits correspond to typical oscillating and rotating orbits, respectively. Aligned with the stability results, the reduced ODE model accurately captures the nonlinear evolution for these orbits. This again supports the conclusion that the reduced ODE is an accurate (qualitatively and quantitatively) depiction, not only for the statics and stability (as seen earlier), but also for the dynamics of vortex orbits in the torus.

In Fig. 14 we depict the dynamics ensuing from the destabilization of unstable dipole configurations. Specifically, Figs. 14(a) and 14(b) depict one period for an oscillating and a rotating orbit, respectively. As discussed before, the horizontal dipole-in steady state corresponds to a saddle (cf. phase spaces of Fig. 7) whose separatrices separate regions with oscillating and rotating orbits. The oscillating orbit was obtained by slightly and symmetrically perturbing the vortices in the poloidal direction. Similarly, the rotating orbit was obtained by slightly and symmetrically perturbing in the toroidal direction. Figure 14(c) depicts a typical destabilization of the diagonal dipole. In this case, as the symmetry is already broken from the steady state, the destabilization

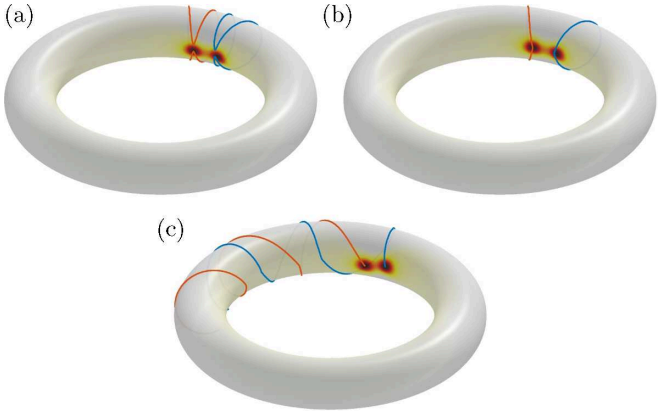

FIG. 14. Dynamics ensuing from the destabilization of unstable dipole configurations: one period of (a) oscillating and (b) rotating dipole-in orbits close to the separatrix. The oscillating and rotating orbits were obtained by slightly shifting the vortices in the poloidal and toroidal directions, respectively. (c) Destabilization of the diagonal dipole. All cases correspond to $\mu = 5$, $R = 12$, and $\alpha = 0.2$. The colored surface depicts the initial density and the overlaid curves correspond to the trajectory traces from the negative (red) and positive (blue) vortices. [See Figs. 14(a)–14(c) in the Supplemental Material [48] for movies depicting the evolution of the density and phase, respectively.]

dynamics follows windings along both toroidal and poloidal directions. Since the diagonal dipole has an angle that is close to horizontal (toroidal), the dipole has a relatively fast poloidal speed and a relatively slow toroidal drift. The ensuing orbit will be generically a quasiperiodic orbit (unless the windings along the toroidal and poloidal directions are commensurate with each other).

B. Vortex quadrupoles

1. *Steady states*

While there exist only four steady-state vortex dipoles, as the number of vortices is increased, a larger assortment of possibilities arises. Motivated by the remarkable agreement of the reduced ODE model with the original NLS equation model, we have proceeded to leverage its use to identify possible quadrupole solutions in the full NLS equation model. Even when using the reduced ODE model, an exhaustive (ordered) search for quadrupoles (and higher-order tuples), as it was performed for the vortex dipoles in Sec. III A, is a challenging task. This is because of the commonly referred to curse of dimensionality. While for the vortex dipole, after eliminating the toroidal translational invariance, the reduced ODE model is left with three degrees of freedom, for the vortex quadrupole one has (after eliminating the translational invariance) seven degrees of freedom. Therefore, an exhaustive search over the whole phase space is computationally prohibitive. Thus, we revert to randomly sampling initial conditions over this seven-dimensional space (for all other parameters fixed, namely, R and α) and using a standard fixed-point iteration (nonlinear least squares with a Levenberg-Marquardt algorithm) to converge to the closest steady-state solution. Using several million initial conditions, we were able to detect 16 distinct

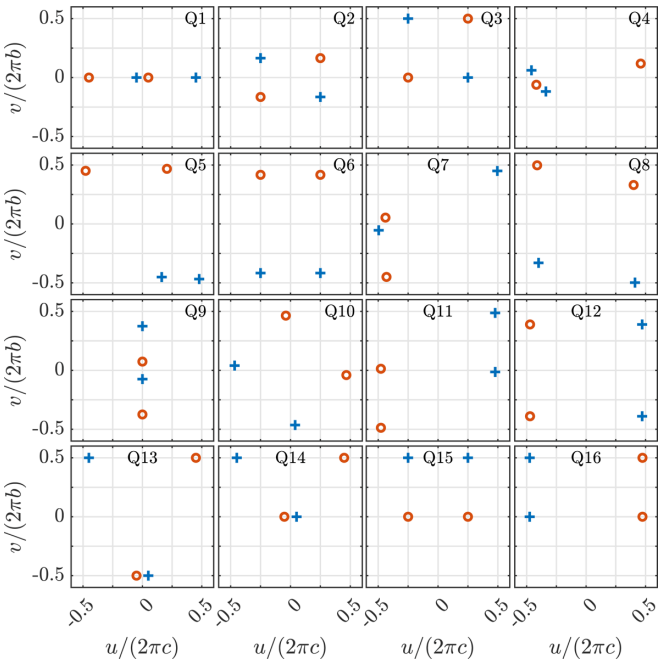

FIG. 15. Quadrupole solutions from the ODE model for $R = 12$ and $\alpha = 0.5$. These solutions are ordered from least unstable to most unstable (see Fig. 16 for the corresponding spectra). Positive (negative) vortices are depicted with the blue (red) crosses (circles). Vortex locations are plotted in scaled isothermal coordinates.

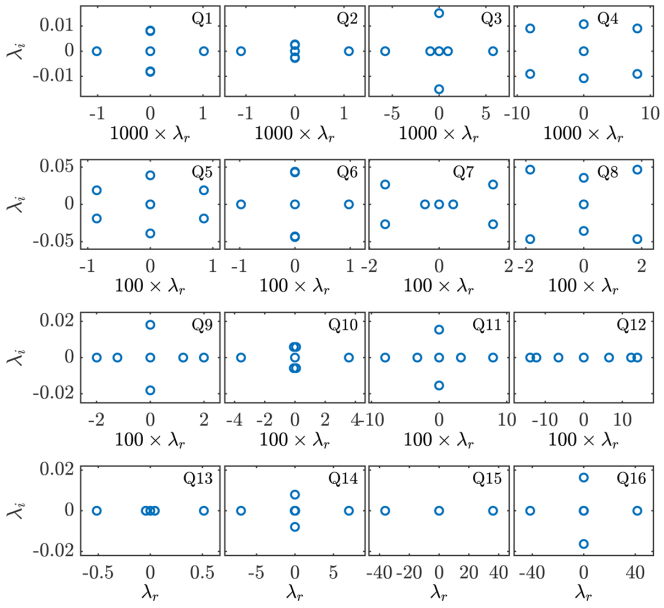

FIG. 16. Stability spectra (λ_r, λ_i) corresponding to the quadrupole solutions of Fig. 15 obtained from the reduced ODE model. Note that each row of panels has a different scaling for the real part of the eigenvalue as indicated. The configurations are ordered from least unstable to most unstable. In particular, the first three quadrupoles present a very weak instability of $O(10^{-3})$ for these values of the parameters ($R = 12$ and $\alpha = 0.5$).

quadrupole configurations as depicted in Fig. 15 for $R = 12$ and $\alpha = 0.5$. By distinct we mean here that we have eliminated all the equivalent solutions (not only through toroidal translations but also) through symmetries associated with reflections across $\theta = 0$, symmetries associated with reversing the vortex charges, and permutations of the vortex labels. We have therefore obtained a rich palette of quadrupole solutions as depicted in Fig. 15. It is worth mentioning that these solutions have been ordered Q1, . . . ,Q16 from the least unstable to the most unstable one (for the parameters at hand, namely, $R = 12$ and $\alpha = 0.5$). They include horizontally (Q1) and vertically aligned quadrupoles (Q9), rectangular quadrupoles (Q2, Q3, Q6, Q12, and Q16), rhomboidal quadrupoles (Q8, Q10, Q11, and Q15), trapezoidal quadrupoles (Q5, Q13, and Q14), and, somewhat surprisingly, irregular quadrupoles (Q4 and Q7).

2. *Stability*

Let us now comment on the stability for the obtained quadrupole solutions. We start by analyzing the stability obtained from the reduced ODE model. Figure 16 depicts the ODE spectra associated with the 16 distinct quadrupoles depicted in Fig. 15. As mentioned above, the solutions have been ordered from least unstable to most unstable by using the maximal real part for all eigenvalues $\max(\lambda_r)$. It is important to stress that the eigenvalues, and thus the ordering of the quadrupole solutions as we have posited it, change as the parameters of the system are varied. Therefore, it is relevant to look at the associated spectra as the parameters are varied. Particularly revealing for some of these solutions is the continuation of spectra as the torus aspect ratio α is varied. For compactness, we only show these full ODE spectra for the first three quadrupole configurations in Fig. 17. These configurations, as shown in Fig. 16, have a very weak instability $[\max(\lambda_r) < 0.01]$ for $\alpha = 0.5$ (and $R = 12$) and thus are potential candidates to be completely stable as the parameters are varied. As Fig. 17 shows, for $R = 12$, Q2 is always unstable; however, this instability is rather weak as it merely reaches $\max(\lambda_r) \simeq 0.0017$ around $\alpha \simeq 0.73$. On the other hand, not only are Q1 and Q3 weakly unstable for most values of α, but, importantly, they can be rendered stable on respective windows of the parameter α. Specifically, as the figure shows, for $R = 12$, the Q1 solution is stable for $0.84 \lesssim \alpha < 1$ and the Q2 solution is stable for the narrow interval $0.656 \lesssim \alpha \lesssim 0.664$ [see the inset in Fig. 17(c) for Q3]. In addition to the stability windows for Q1 and Q3, it is also worth mentioning that the reduced model predicts that a few quadrupole solutions have relatively weak instabilities. For instance, as it can be seen in Fig. 16, the quadrupoles Q1 and Q2 have a $\max(\lambda_r) \simeq 10^{-3}$, while Q3 has a $\max(\lambda_r) \simeq 6 \times 10^{-3}$ and Q4 has a $\max(\lambda_r) \simeq 9 \times 10^{-3}$, all for $\alpha = 0.5$ and $R = 12$. Therefore, for the parameter combinations that we explored, although we only found Q1 and Q3 to possess stability windows, the rather weak instabilities presented by about half of the quadrupole configurations $[\max(\lambda_r) < 0.02]$ suggest that they have the potential to be long-lived solutions in the original NLS equation (cf. the dynamics for Q1 in Sec. III B 3) and the corresponding physical experiments.

We now turn to the study of the stability of the quadrupole configurations from the full NLS equation model and compare the latter with the results from the reduced ODE model. In particular, Fig. 18 shows the stability results from both the

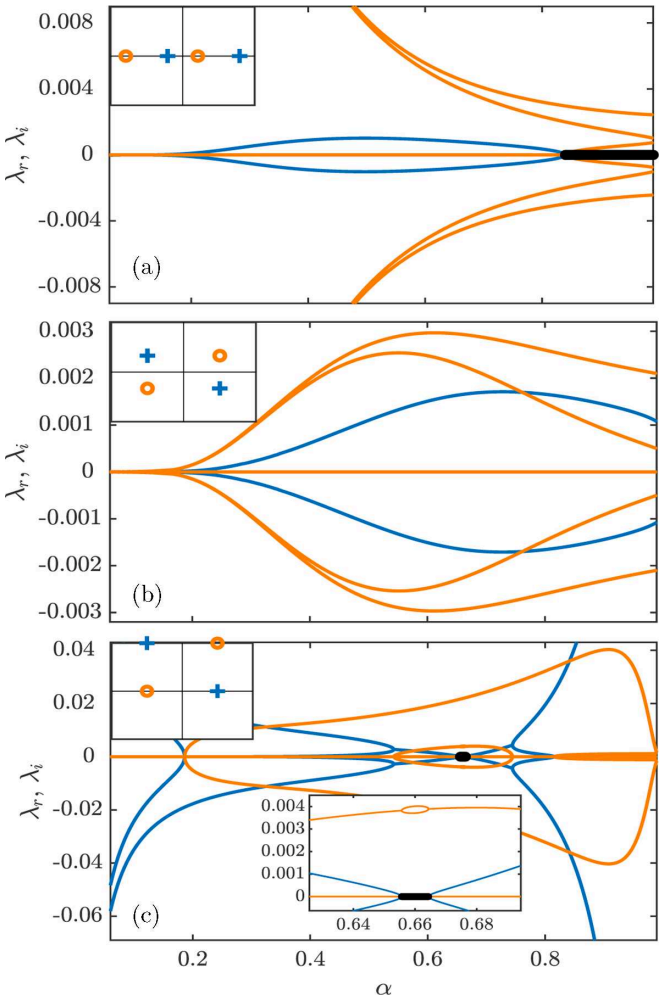

FIG. 17. Stability spectra as α is varied in the reduced ODE model for the (a) first (Q1), (b) second (Q2), and (c) third (Q3) quadrupole solutions (see Fig. 15) for $R = 12$. Blue (dark) and orange (light) curves correspond to the real (λ_r) and imaginary (λ_i) parts of the eigenvalue. The top left insets depict the configurations for $\alpha = 0.5$. The Q1 and Q3 quadrupole solutions were the only ones found to have stability intervals as α was varied. These stability intervals are depicted by the thick black lines. The bottom inset for Q3 corresponds to a close-up around the stability interval.

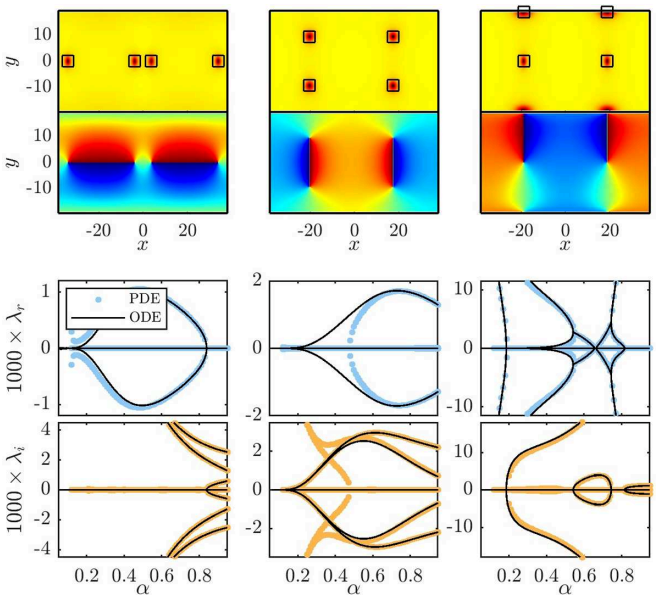

FIG. 18. Comparing full model (PDE) and reduced model (ODE) spectra for quadrupoles Q1 (left), Q2 (middle), and Q3 (right) as α is varied for $R = 12$ and $\mu = 1$. The layout and parameters are similar to those of Fig. 11.

reduced ODE and the full NLS equation models for the Q1, Q2, and Q3 configurations as α is varied for $R = 12$ and $\mu = 1$. It is remarkable that, even with this moderately small value of μ ($\mu = 1$), the reduced ODE model is capable of recovering the main stability eigenvalues of the full NLS equation for most parameter values. For instance, the complicated bifurcation scenario displayed by Q3 is perfectly captured by the ODE model (including the bifurcation leading to the narrow stability window around $\alpha \simeq 0.66$). In general, we expect that the ODE model is able to properly capture the instabilities corresponding to the destabilization of the vortex positions. However, it is conceivable that there exist instabilities for full NLS equation solutions that are not captured by the reduced ODE model as the corresponding eigendirections might not be part of the space spanned by the latter. Surprisingly, however, as it can be observed from the spectrum of Q2 in Fig. 18, the NLS configurations seems to stabilize for $\alpha \lesssim 0.48$, while the reduced ODE model predicts that the solution is (weakly) unstable for all values of α. This tends to suggest that the actual spatial extent of the vortices, and their mutual interaction through the curvature of the background, may be responsible for this stabilization since the point-vortex model, relevant for the $\mu \to \infty$ limit, does not display this stabilization effect.

Finally, in Fig. 19 we depict the convergence of the stability spectra for the Q1 and Q3 dipoles as μ is increased for $R = 12$ and $\alpha = 0.4$ and 0.7. As it was the case for the vortex dipoles, the convergence between the original NLS equation model and the reduced ODE model as μ increases is extremely good. In fact, even for moderate values of $\mu \approx 2$ the discrepancy between the maximum real parts of the eigenvalues for the full NLS equation model and the ODE model is less than 4% in all the examined cases. Furthermore, the qualitative stability conclusions do not appear to change over μ for the cases and intervals considered.

3. Dynamics

Let us now follow the destabilization dynamics for quadrupole configurations. Figure 20 depicts the dynamics ensuing for the first three quadrupole steady-state configurations (Q1, Q2, and Q3). In particular, Fig. 20(a) depicts the destabilization of the Q2 dipole. The corresponding orbit follows the unstable manifold of this unstable saddle fixed point and seems to return along the stable manifold suggesting, as it was the case for the horizontal dipoles (cf. Fig. 7), the existence of a homoclinic orbit. Figure 20(b) depicts a typical destabilization for the Q3 dipole. Finally, Figs. 20(c) and 20(d) depict the dynamics ensuing from perturbing the Q1 quadrupole. It is important to stress that the values of α [$\alpha = 0.5$ Fig. 20(c) and $\alpha = 0.7$ for Fig. 20(d)] are *below* the

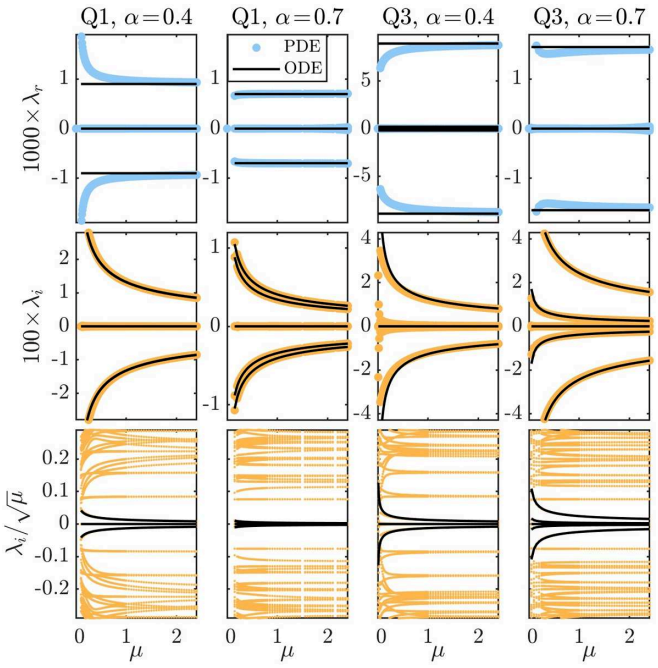

FIG. 19. Convergence of the stability spectra for the Q1 and Q3 quadrupole configurations as the chemical potential μ is increased for $R = 12$ and $\alpha = 0.4$ and 0.7 as indicated. The layout is the same as in Fig. 10.

stability window that starts around $0.84 \lesssim \alpha$. Therefore, for these values of the parameters, the Q1 quadrupole is unstable. However, when following the perturbed dynamics for times of the order of several thousands [see Fig. 20(c)] the vortices seem to trace a neutrally stable periodic (center) orbit. The reason for this apparent stability stems from the fact that the Q1 quadrupole is unstable but that its instability eigenvalue is rather weak [$\max(\lambda_r) \simeq 0.001$; see Fig. 17(a)]. The instability for the Q1 quadrupole is indeed manifested for longer times as shown in Fig. 20(d), where the vortices slowly begin to spiral out for $t > 10\,000$ and finally engage in an apparent irregular dance for $t > 15\,000$.

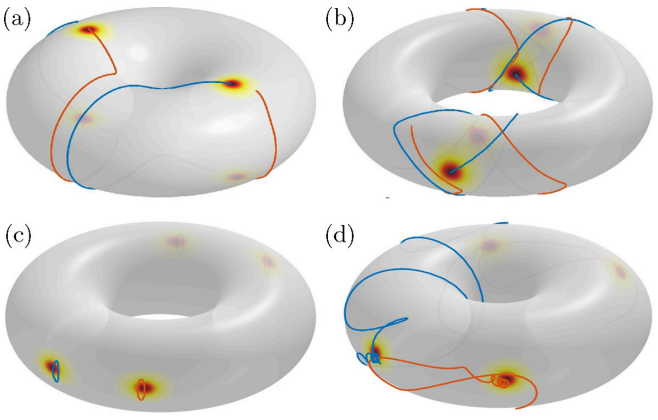

FIG. 20. Dynamics ensuing from the destabilization of unstable quadrupole configurations for $R = 12$ and $\mu = 1$. (a) Destabilization of the Q2 quadrupole for $\alpha = 0.7$ giving rise to approximately (about half of) a periodic orbit. (b) Destabilization of the Q3 quadrupole for $\alpha = 0.4$. (c) Weakly unstable periodic orbit for a perturbed Q1 quadrupole for $\alpha = 0.5$ for $0 \leqslant t \leqslant 4000$. (d) Weakly stable periodic orbit for a perturbed Q1 quadrupole for $\alpha = 0.7$ eventually destabilizes for longer times $0 \leqslant t \leqslant 28\,000$. The colored surface depicts the initial density and the overlaid curves correspond to the trajectory traces from the negative (red) and positive (blue) vortices. [See Figs. 20(a)–20(d) in the Supplemental Material [48] for movies depicting the evolution of the density and phase, respectively.]

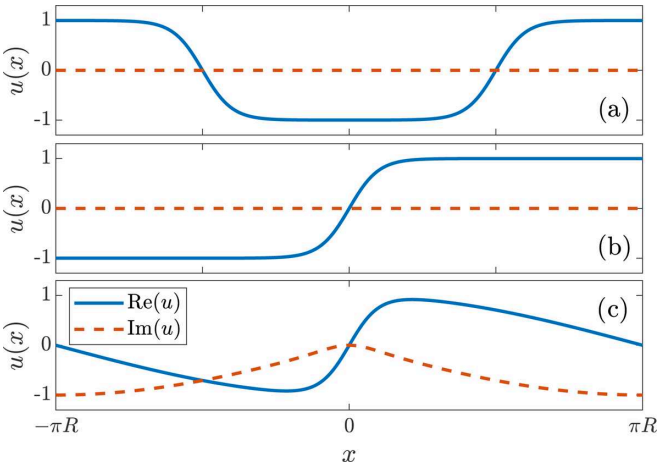

FIG. 21. Dark solitons and windings. (a) Two dark solitons always respect the periodicity of the domain. (b) A single dark soliton without extra phase winding does not satisfy the periodic boundary conditions. (c) In contrast, the addition of an appropriate phase winding allows for the single dark soliton to be periodic on the domain. Blue solid curves depict the real part of the solution while red dashed curves depict the imaginary parts.

Although in the case of the dipole the motions we have encountered seem to be prototypically quasiperiodic, in the case of quadrupole configurations, there are six degrees of freedom and despite the presence of a conserved energy, there is potential for complex (chaotic) behavior. Studies along these lines are outside the scope of the present paper and are left for future work.

C. Dark-soliton stripes

Finally, let us briefly examine some of the properties of dark-soliton-stripe configurations and their connection with some of the vortex configurations of the previous sections. For instance, as Fig. 3 suggests, as μ is decreased, the horizontal dipole-in configuration seems to degenerate, as the vortices eventually merge, into a *single* horizontal (toroidal) stripe. It is important to first understand the nature of this single stripe. As is the case for vortices, in order to satisfy the periodicity of the domain, dark-soliton stripes should appear in pairs as each one will contribute to a π phase jump for a total of a 2π phase jump conducive to a periodic domain. For instance, in Fig. 21(a) we depict the two-soliton solution along the toroidal domain that is naturally periodic. However, a single dark soliton [see Fig. 21(b)] is not periodic on the domain. Nonetheless, it is possible to seed a single dark soliton if one adds a winding to add (or counter) the π phase jump of a single stripe. In fact, if one takes a single dark soliton along the toroidal direction (or, similarly, in the poloidal direction)

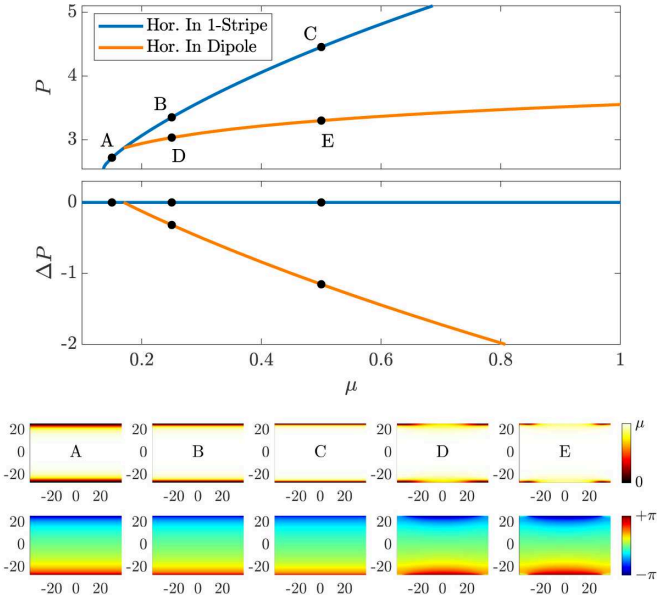

FIG. 22. Bifurcation between the horizontal-in single dark-soliton stripe and the horizontal dipole-in configuration. The top panel depicts the power for both solutions as a function of μ for $\alpha = 0.7$ and $R = 12$. The second panel depicts the power difference between the two solutions. The last two row of panels depict the density (top subpanels) and phase (bottom subpanels) of the solutions in Cartesian coordinates at the points indicated in the first panel, namely, $\mu = 0.15$ for point A, $\mu = 0.25$ for points B and D, and $\mu = 0.5$ for points C and E.

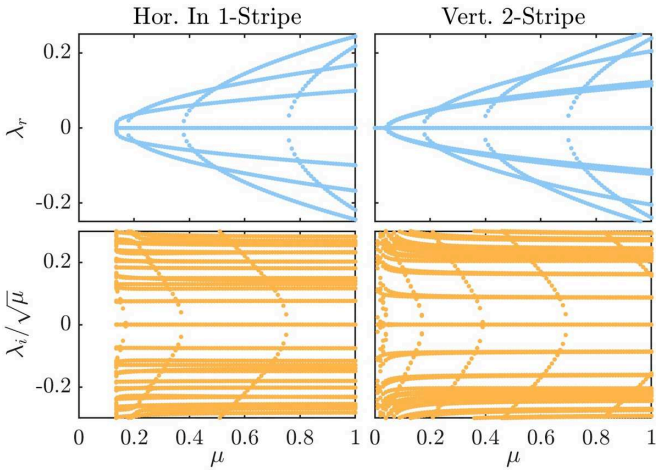

FIG. 23. Bifurcation spectra for the horizontal-in single stripe for $\alpha = 0.7$ (left) and the vertical double stripe for $\alpha = 0.4$ (right). Sample instability eigenfunctions are shown in Fig. 24.

and imprints the phase $-2\pi/2\pi R$ on it, the result is a periodic function [see Fig. 21(c)]. Therefore, it is in principle possible to construct single horizontal stripe configurations that are consonant with the periodicity by adding a vertical winding $W_y = n + 1/2$ (with n integer). Likewise, single vertical stripes are possible when adding a half-integer horizontal winding $W_x = n + 1/2$. In fact, it is possible to construct any number of *odd* stripes by adding half-integer windings. On the other hand, similarly to our discussion for vortices, from the perspective of the torus periodicity, it is possible for our system to feature even numbers of parallel dark stripes (without external winding) whose total phase change adds up to a multiple of 2π.

In Fig. 22 we depict more details of the bifurcation between the horizontal-in single stripe and the corresponding dipole solutions. In particular, we follow the effective power of the solutions by computing

$$P = \iint_0^{2\pi} (\mu - |\psi|^2) dS, \tag{20}$$

where the surface element on the torus is $dS = |\hat{\phi} \times \hat{\theta}| d\theta d\phi$. Here circumflexes denote the unit vectors in the different (toroidal and poloidal) directions. Thus, $|\hat{\phi} \times \hat{\theta}| = R + r\cos(\theta)$. This effective power measures the volume of the hole that is depleted of density due to the presence of the dark-soliton stripes. The associated quantity is physically meaningful as the atom number associated with the density depletion in BECs. As the top two panels of Fig. 22 evidence, the horizontal dipole-in configuration bifurcates from the horizontal-in single stripe at $\mu \approx 0.17$. The bottom two rows of panels in Fig. 22 depict sample solutions before and after the bifurcation. The phase panels indicate that the stripe has indeed an extra vertical winding of $W_y = -1/2$ and that the vortices of the dipole merge as μ decreases towards the bifurcation at $\mu \approx 0.17$.

In a similar fashion, as the horizontal dipole-in configuration bifurcates from the single horizontal-in stripe, multiple other bifurcations are present involving single and double (and triple, etc.), in and out, vertical and horizontal dark stripes and vortex configurations. In fact, we have observed (not shown here) mixed bifurcations where, as μ increases, a double horizontal stripe, containing an in and an out stripe, first features a bifurcation towards a mixed state containing a vortex out configuration and a stripe which, subsequently, after a further increase in μ, displays a bifurcation for the horizontal-in stripe leading to a multivortex state. An in-depth analysis of the possible bifurcations involving the above configurations, albeit interesting, falls outside the scope of the present work. Nonetheless, we present here a collection of examples that showcase some of the most basic bifurcations and ensuing dynamics involving dark-soliton stripes.

Figure 23 depicts the bifurcation spectra for the horizontal-in single stripe (left) and the vertical double stripe (right). The spectra for both stripe configurations display a series (cascade) of bifurcations as μ departs from zero. Each bifurcation is associated with the creation of an offspring configuration where each stripe is replaced by vortices. The higher the bifurcation is in the cascade, the more vortices are produced. This cascading bifurcation is akin to the bifurcation of dark-soliton stripes and rings in parabolically trapped BECs as reported, e.g., in Ref. [49]. In Fig. 24 we portray elements of these bifurcations by perturbing the stripe steady states by the eigenfunction corresponding to the most unstable eigenvalue as shown in Fig. 24. The figure depicts the stripe steady states (left), their corresponding most unstable eigenfunction (middle), and the steady state perturbed by the eigenfunction (right). In these cases we normalized the eigenfunction such that its maximum density (norm) coincided with the

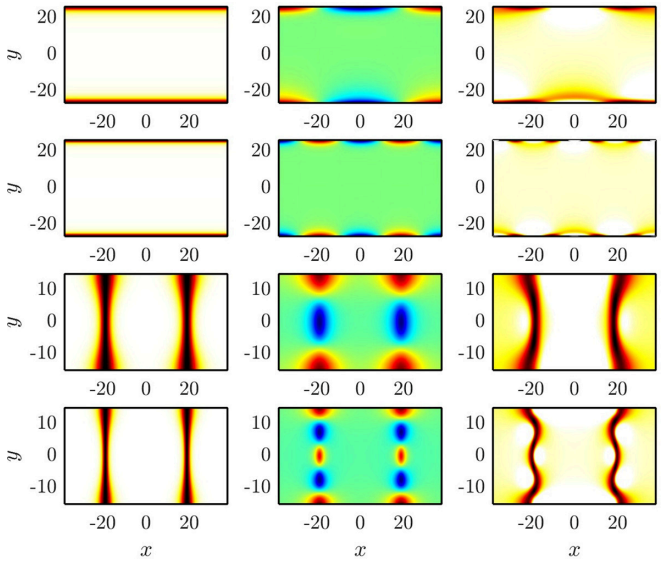

FIG. 24. Effects of the most unstable eigenfunctions for stripe configurations for $R = 12$. The left panels depict the steady-state configuration and the middle panels their corresponding (real part of the) most unstable eigenfunction. The right panels depict the stripe configuration after a (large) perturbation with the most unstable eigenfunction. All states are plotted in Cartesian coordinates. The first and second rows show the horizontal-in single stripe for $\alpha = 0.7$ and $\mu = 0.25$ and 0.5, respectively, and the third and fourth rows the vertical double stripe for $\alpha = 0.4$ and $\mu = 0.1$ and 0.3, respectively. The corresponding evolution dynamics (for a much smaller perturbation strength) are depicted in Fig. 25.

chemical potential μ of the steady state and we added it using a large perturbation prefactor equal to 2. This was done for presentation purposes to exaggerate the visual effects of the perturbation (for the actual dynamical runs presented in Fig. 25 we used a small prefactor for the relevant perturbation of 10^{-3}). As Fig. 24 shows, the different eigenfunctions bend the stripes into snaking modes with a higher number of relevant undulations as μ increases and the higher bifurcations in the cascade are reached. Specifically, the first two rows in the figure present the first two unstable modes of the horizontal-in single stripe, each giving rise to an aligned quadrupole and hexapole, respectively, after the system is left to evolve as depicted in the first two rows of Fig. 25. On the other hand, the third and fourth rows in Fig. 24 depict the first two excited modes of the double vertical stripe which in this case give rise to a Q2-like quadrupole (see $t = 250$) and an octupole (see $t = 120$), respectively. The corresponding destabilization dynamics are shown in the third and fourth rows of Fig. 25. Note that the destabilization along the second mode of the vertical double stripe (fourth row of panels) initially generates a vortex octupole ($t = 120$). However, as time progresses, the outer two vortex pairs on each side of the torus merge and produce two "lumps" that travel, in opposite directions, along the toroidal direction until they are eventually destroyed and contribute to background radiation. These lumps correspond to solitonic structures dubbed Jones-Roberts solitons [50], which have been observed in recent BEC experiments [51]. These are quite interesting to explore in their own right in the realm of traveling solutions in the torus setting. While our exploration herein has been restricted (due to their extensive wealth, as we have tried to argue) to stationary states, it does not escape us that such traveling waveforms, including ones involving vorticity, are of particular interest in their own right for future studies.

IV. CONCLUSION AND OUTLOOK

In this work we have attempted to give a systematic and extensive (although by no means exhaustive) study of the existence, stability, and dynamics of dark and vortical structures in the nonlinear Schrödinger equation on the surface of a torus as the torus aspect ratio α and the chemical potential μ of the solutions are varied. We chiefly study vortex dipoles and quadrupoles but also touch upon dark-soliton stripes and their connections to the former (through bifurcation cascades). To obtain an understanding of the statics, stability, and dynamics of vortex configurations of the full NLS equation model, we have leveraged the key insights offered by a remarkably successful (as we illustrated) reduced particle model, introduced

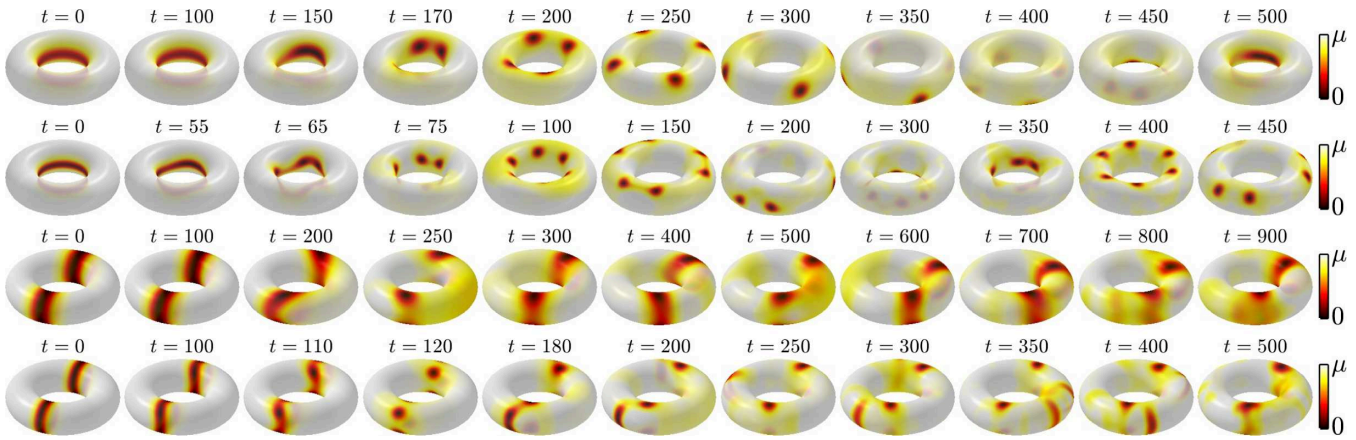

FIG. 25. Evolution dynamics of unstable stripe configurations for $R = 12$. All initial conditions are taken as the stationary stripe configuration perturbed by 10^{-3} times the most instable eigenfunction. The first and second rows show the horizontal-in single stripe for $\alpha = 0.7$ and $\mu = 0.25$ and 0.5, respectively, and the third and fourth rows the vertical double stripe for $\alpha = 0.4$ and $\mu = 0.1$ and 0.3, respectively. [See Figs. 15(a)–15(d) in the Supplemental Material [48] for movies depicting the evolution of the density and phase, respectively.]

in Ref. [43], based upon assuming vortices without internal structure (i.e., point vortices) that incorporates both vortex-vortex interactions and the effects of space curvature on the surface of the torus. We have also considered numerically the waveforms including vertical or horizontal phase windings. We showed that this (fundamental within this setting) reduced particle model is extremely accurate at predicting the statics, stability, and dynamics of dipole configurations even for moderate values of the chemical potential. We have also discussed the potential limitations of the model in regimes of low chemical potential or, in some cases, small enough aspect ratios. The balance between vortex-vortex interactions and the curvature effects gives rise to four different types of dipole solutions: (i) the vertical dipole-in configuration, (ii) the horizontal dipole-in configuration (vortices close to the inside part of the torus), (iii) the horizontal dipole-out configuration (vortices close to the outside part of the torus), and (iv) the diagonal dipole configuration. The vertical dipole-in and horizontal dipole-out configurations are (neutrally) stable for a wide range of parameters, while the horizontal dipole-out configuration and diagonal dipoles are chiefly unstable. The source of the relevant (stability or) instability via an eigendirection associated with the relative motion of the vortices has been identified and the related unstable dynamics also elucidated. Nonetheless, for thick tori (large torus aspect ratio) it is possible to stabilize the diagonal vortex dipole for sufficiently large chemical potentials.

We also explored vortex quadrupole configurations. We found 16 different quadrupoles ranging from horizontally and vertically aligned quadrupoles to rectangular and rhomboidal quadrupoles to trapezoidal quadrupoles and even to some irregular quadrupoles. All these solutions were continued and monitored for stability as the torus aspect ratio is varied within the reduced ODE model. Out of these 16 quadrupoles we found two that exhibited windows of stability, upon variations of the aspect ratio. We also found a handful of stationary quadrupole solutions with very weak instabilities, indicating that it may be possible to observe them as long-lived solutions at the full NLS equation level. Relevant stability considerations were also presented at the PDE level and indeed, surprisingly, it was found that some configurations, such as the rectangular Q2, could be more robust at the latter level and indeed genuinely stable for sizable parametric intervals therein. Finally, we briefly touched upon dark-soliton-stripe configurations. These stripes can be single or double (or triple, etc.), horizontal or vertical, and centered about the inner or outer side of the torus. Particularly interesting are the bifurcations of vortex configurations from these stripes as μ increases from the low-density limit in a series of bifurcating cascades corresponding to an increasing number of vortices, reminiscent of ones emerging for stripe as well as ring configurations in regular two-dimensional parabolically confined BECs.

A natural extension of this work would be to study vortex configurations with a higher number of vortices. It would be indeed interesting to see if configurations for a higher number of vortices can be rendered stable for the right parameter windows in a manner akin to what we detected for a couple of the quadrupole configurations (Q1 and Q3). It is likely that configurations with a higher number of vortices will be difficult to stabilize. Indeed, we encountered some such configurations transiently in our dynamics (e.g., stemming from unstable stripes). It would also be interesting to understand in more detail how some full NLS equation solutions seem to be more stable than their effective ODE model counterparts (cf. Q2 quadrupole). On the other hand, it would also be relevant to study in more detail the bifurcation cascades between the different stripes—single or double (or triple, etc.), in or out, vertical or horizontal—and stationary vortex configurations. This is an intricate endeavor as these cascades are very much dependent on the aspect ratio of the torus (α). For instance, a very thin torus ($\alpha \to 0$) will preferentially promote the merger of vortices along the poloidal direction. However, when the two torus radii are similar ($\alpha \to 1$) both mergers along toroidal and poloidal directions will nontrivially compete. Finally, further leveraging of the reduced ODE model could be employed to study the existence and stability of periodic vortex orbits in a manner akin to vortex choreography in the plane [52]. Indeed, an example of such periodic solutions, returning to themselves upon running around the torus, are traveling solutions, such as the lump ones spontaneously encountered herein. Given their potential connection to so-called Kadomtsev-Petviashvili lumps [53], this is an interesting direction in its own right. Indeed, given the success of the particle model herein, exploring additional directions such as the potential ordered and chaotic orbits [54] at the low-dimensional dynamical system level could also hold some appeal. Finally, we hope that this fruitful comparison of the ODE and PDE dynamics at the level of the torus will springboard further related comparative studies in the context of other nontrivial geometric settings, including spherical, cylindrical, and conical shells, among others.

ACKNOWLEDGMENTS

We acknowledge A. L. Fetter for useful comments. J.D. gratefully acknowledges computing support based on the Army Research Office ARO-DURIP Grant No. W911NF-15-1-0403. R.C.-G. gratefully acknowledges support from the U.S. National Science Foundation under Grants No. PHY-1603058 and No. PHY-2110038. This material is based upon work supported by the U.S. National Science Foundation under Grants No. DMS-1809074 and No. PHY-2110030 (P.G.K.).

[1] L. P. Pitaevskii and S. Stringari, *Bose-Einstein Condensation and Superfluidity* (Oxford University Press, Oxford, 2016).

[2] C. J. Pethick and H. Smith, *Bose-Einstein Condensation in Dilute Gases* (Cambridge University Press, Cambridge, 2002).

[3] P. G. Kevrekidis, D. J. Frantzeskakis, and R. Carretero-González, *The Defocusing Nonlinear Schrödinger Equation* (SIAM, Philadelphia, 2015).

[4] *Emergent Nonlinear Phenomena in Bose-Einstein Condensates: Theory and Experiment*, edited by P. G. Kevrekidis, D. J. Frantzeskakis, and R. Carretero-González (Springer, Berlin,

2008); R. Carretero-González, D. J. Frantzeskakis, and P. G. Kevrekidis, Nonlinearity **21**, R139 (2008).
[5] See, e.g., N. P. Proukakis, in *Emergent Nonlinear Phenomena in Bose-Einstein Condensates: Theory and Experiment* (Ref. [4]), p. 353.
[6] L. Khaykovich, F. Schreck, G. Ferrari, T. Bourdel, J. Cubizolles, L. D. Carr, Y. Castin, and C. Salomon, Science **296**, 1290 (2002).
[7] K. E. Strecker, G. B. Partridge, A. G. Truscott, and R. G. Hulet, Nature (London) **417**, 150 (2002).
[8] S. L. Cornish, S. T. Thompson, and C. E. Wieman, Phys. Rev. Lett. **96**, 170401 (2006).
[9] S. Burger, K. Bongs, S. Dettmer, W. Ertmer, K. Sengstock, A. Sanpera, G. V. Shlyapnikov, and M. Lewenstein, Phys. Rev. Lett. **83**, 5198 (1999).
[10] J. Denschlag, J. E. Simsarian, D. L. Feder, C. W. Clark, L. A. Collins, J. Cubizolles, L. Deng, E. W. Hangley, K. Helmerson, W. P. Reinhardt, S. L. Rolston, B. I. Schneider, and W. D. Phillips, Science **287**, 97 (2000).
[11] C. Becker, S. Stellmer, P. Soltan-Panahi, S. Dörscher, M. Baumert, E.-M. Richter, J. Kronjäger, K. Bongs, and K. Sengstock, Nat. Phys. **4**, 496 (2008).
[12] A. Weller, J. P. Ronzheimer, C. Gross, J. Esteve, M. K. Oberthaler, D. J. Frantzeskakis, G. Theocharis, and P. G. Kevrekidis, Phys. Rev. Lett. **101**, 130401 (2008).
[13] P. Engels and C. Atherton, Phys. Rev. Lett. **99**, 160405 (2007).
[14] S. Stellmer, C. Becker, P. Soltan-Panahi, E.-M. Richter, S. Dörscher, M. Baumert, J. Kronjäger, K. Bongs, and K. Sengstock, Phys. Rev. Lett. **101**, 120406 (2008).
[15] G. Theocharis, A. Weller, J. P. Ronzheimer, C. Gross, M. K. Oberthaler, P. G. Kevrekidis, and D. J. Frantzeskakis, Phys. Rev. A **81**, 063604 (2010).
[16] D. J. Frantzeskakis, J. Phys. A: Math. Theor. **43**, 213001 (2010).
[17] O. Morsch and M. Oberthaler, Rev. Mod. Phys. **78**, 179 (2006).
[18] P. G. Kevrekidis and D. J. Frantzeskakis, Rev. Phys. **1**, 140 (2016).
[19] A. L. Fetter and A. A. Svidzinsky, J. Phys.: Condens. Matter **13**, R135 (2001).
[20] A. L. Fetter, Rev. Mod. Phys. **81**, 647 (2009).
[21] I. Shomroni, E. Lahoud, S. Levy, and J. Steinhauer, Nat. Phys. **5**, 193 (2009).
[22] S. Komineas, Eur. Phys. J.: Spec. Top. **147**, 133 (2007).
[23] K. Padavić, K. Sun, C. Lannert, and S. Vishveshwara, Phys. Rev. A **102**, 043305 (2020).
[24] S. J. Bereta, M. A. Caracanhas, and A. L. Fetter, Phys. Rev. A **103**, 053306 (2021).
[25] B. Rhyno, N. Lundblad, D. C. Aveline, C. Lannert, and S. Vishveshwara, Phys. Rev. A **104**, 063310 (2021).
[26] A. Tononi and L. Salasnich, Phys. Rev. Lett. **123**, 160403 (2019).
[27] N.-E. Guenther, P. Massignan, and A. L. Fetter, Phys. Rev. A **96**, 063608 (2017).
[28] P. Massignan and A. L. Fetter, Phys. Rev. A **99**, 063602 (2019).
[29] H. Lamb, *Hydrodynamics*, 6th ed. (Cambridge University Press, Cambridge, 1932).
[30] P. K. Newton, *The N-Vortex Problem* (Springer, Berlin, 2001).
[31] A. M. Turner, V. Vitelli, and D. R. Nelson, Rev. Mod. Phys. **82**, 1301 (2010).
[32] E. R. Elliott, M. C. Krutzik, J. R. Williams, R. J. Thompson, and D. C. Aveline, npj Microgravity **4**, 16 (2018).
[33] M. Meister, A. Roura, E. M. Rasel, and W. P. Schleich, New J. Phys. **21**, 013039 (2019).
[34] G. Condon, M. Rabault, B. Barrett, L. Chichet, R. Arguel, H. Eneriz-Imaz, D. Naik, A. Bertoldi, B. Battelier, P. Bouyer, and A. Landragin, Phys. Rev. Lett. **123**, 240402 (2019).
[35] D. C. Aveline, J. R. Williams, E. R. Elliott, C. Dutenhoffer, J. R. Kellogg, J. M. Kohel, N. E. Lay, K. Oudrhiri, R. F. Shotwell, N. Yu, and R. J. Thompson, Nature (London) **582**, 193 (2020).
[36] N. Lundblad, R. A. Carollo, C. Lannert, M. J. Gold, X. Jiang, D. Paseltiner, N. Sergay, and D. C. Aveline, npj Microgravity **5**, 30 (2019).
[37] K. Frye *et al.*, EPJ Quantum Technol. **8**, 1 (2021).
[38] B. M. Garraway and H. Perrin, J. Phys. B **49**, 172001 (2016).
[39] R. A. Carollo, D. C. Aveline, B. Rhyno, S. Vishveshwara, C. Lannert, J. D. Murphree, E. R. Elliott, J. R. Williams, R. J. Thompson, and N. Lund, Nature **606**, 281 (2022).
[40] O. Zobay and B. M. Garraway, Phys. Rev. Lett. **86**, 1195 (2001).
[41] K. Henderson, C. Ryu, C. MacCormick, and M. G. Boshier, New J. Phys. **11**, 043030 (2009).
[42] H. Kim, G. Zhu, J. V. Porto, and M. Hafezi, Phys. Rev. Lett. **121**, 133002 (2018).
[43] N.-E. Guenther, P. Massignan, and A. L. Fetter, Phys. Rev. A **101**, 053606 (2020).
[44] J. D'Ambroise, P. G. Kevrekidis, and P. Schmelcher, Phys. Lett. A **384**, 126167 (2020).
[45] R. Glowinski and D. C. Sorensen, in *Partial Differential Equations: Modelling and Numerical Simulation*, edited by R. Glowinski and P. Neittaanmäki (Springer, Berlin, 2008), p. 225.
[46] M. A. Stremler and H. Aref, J. Fluid Mech. **392**, 101 (1999).
[47] G. Kirchhoff, Über die stationären elektrischen strömungen in einer gekrümmten leitenden fläche, Monatsber. Akad. Wiss. Berlin, **4**, 487 (1875).
[48] See Supplemental Material at http://link.aps.org/supplemental/10.1103/PhysRevA.105.063325 for movies depicting the evolution of the density and phase.
[49] S. Middelkamp, P. G. Kevrekidis, D. J. Frantzeskakis, R. Carretero-González, and P. Schmelcher, Physica D **240**, 1449 (2011).
[50] C. A. Jones and P. H. Roberts, J. Phys. A Math. Gen. **15**, 2599 (1982).
[51] N. Meyer, H. Proud, M. Perea-Ortiz, C. O'Neale, M. Baumert, M. Holynski, J. Kronjäger, G. Barontini, and K. Bongs, Phys. Rev. Lett. **119**, 150403 (2017).
[52] R. C. Calleja, E. J. Doedel, and C. García-Azpeitia, Regul. Chaot. Dyn. **23**, 595 (2018).
[53] D. Chiron and C. Scheid, Nonlinearity **31**, 2809 (2018).
[54] See, e.g., N. Kyriakopoulos, V. Koukouloyannis, C. Skokos, and P. G. Kevrekidis, Chaos **24**, 024410 (2014).